Harada and Tsujimori
Progress in Earth and Planetary Science (2024) 11:6
https://doi.org/10.1186/s40645-024-00609-y

Progress in Earth and Planetary Science

RESEARCH ARTICLE

Open Access

Methane genesis within olivine-hosted fluid inclusions in dolomitic marble of the Hida Belt, Japan

Hironobu Harada[1*] and Tatsuki Tsujimori[1,2]

Abstract

Abiotic synthesis of hydrocarbon-bearing fluids during geological processes has a significant impact on the evolution of both the Earth's biosphere and the solid Earth. Aqueous alteration of ultramafic rocks, i.e., serpentinization, which forms serpentinite, is one of the geological processes generating abiotic methane (CH_4). However, abiotic CH_4 generation is not limited to the serpentinization of mafic and ultramafic lithologies. Metasedimentary dolomitic marble from the Hida Belt, Japan, is characterized by the presence of forsterite-rich olivine ($Fo_{\sim 89-93}$), and olivine crystals contain abundant fluid inclusions (<1 to 10 μm in size). Raman spectroscopic analyses of olivine-hosted fluid inclusions found that both primary and secondary fluid inclusions contain CH_4, lizardite/chrysotile, and brucite. This indicates that micro-scale interactions between COH fluid and host olivine produced CH_4 through the reduction of CO_2 by H_2 released during local serpentinization within inclusions. Our observation implies that the dolomitic marble has the potential to be a key lithology for the synthesis and storage of abiotic CH_4 in a shallower crustal portion of orogenic belts.

Keywords Dolomitic marble, Fluid inclusion, Olivine, Abiotic methane synthesis, Hida Belt

1 Introduction

Serpentinization of ultramafic rocks is one of the most common abiotic methane (CH_4) generation processes. The process involves the oxidation of ferrous iron contained in primary olivine to ferric iron in secondary minerals, such as serpentine, brucite, and magnetite. Consequently, this oxidation leads to the generation of hydrogen (H_2)-bearing reduced fluids, and the production of CH_4 during serpentinization results from the reduction of CO_2 by these H_2-bearing fluids (e.g., McCollom and Bach 2009; Sleep et al. 2004; Suda et al. 2014). In the natural environment, the presence of hydrocarbon-bearing serpentinite-related fluids has been observed at seafloor hydrothermal fields and ophiolites (e.g., Kelley et al. 2005; Miller et al. 2016; Proskurowski et al. 2008). Although it has been known that shallow low-temperature serpentinization generates H_2-bearing reduced fluids (e.g., Etiope et al. 2011; Etiope and Sherwood Lollar 2013; Kelley et al. 2005; Mottl et al. 2003; Ohara et al. 2012; Proskurowski et al. 2008), Evans (2010) showed that deep high-temperature and high-temperature serpentinization forming antigorite does not generate H_2-bearing reduced fluids. Nevertheless, recent natural observations revealed that high-temperature serpentinization enables the generation of reduced fluids (Boutier et al. 2021; Vitale Brovarone et al. 2020; Zhang et al. 2021). Recent studies have reported abiotic CH_4 synthesis in subduction zone lithologies (Spránitz et al. 2022; Tao et al. 2018; Wang et al. 2022); CH_4-rich fluid inclusions in omphacite from carbonated eclogite of SW Tianshan, China are

*Correspondence:
Hironobu Harada
hironobu.harada.s7@dc.tohoku.ac.jp
[1] Department of Earth Science, Graduate School of Science, Tohoku University, Aoba-ku, Sendai 980-8578, Japan
[2] Center for Northeast Asian Studies, Tohoku University, Aoba-ku, Sendai 980-8576, Japan

considered to be formed by the redox reactions of Fe-bearing carbonates in water (Tao et al. 2018; Wang et al. 2022). Abiotic CH_4 synthesis in such lithologies is rare, and serpentinization has attracted interest as a major abiotic CH_4 production process. However, as reported in this study, abiotic CH_4 production during serpentinization is not limited to the ultramafic lithologies found in abyssal peridotite and ophiolite. Reconnaissance studies for the abiotic CH_4 production in supracrustal metasedimentary rocks in the continental crust have just begun.

In this paper, we present the occurrence of olivine-hosted fluid inclusions containing CH_4 from a dolomitic marble from the Hida Belt, Japan. Based on the mineral inclusions associated with those fluid inclusions, we propose that abiotic CH_4 synthesis in fluid inclusions is not limited to ultramafic lithologies but also occurs in non-ultramafic lithologies within the middle crustal section of the continental margin.

2 Geological background

The Hida Belt of central Japan (Fig. 1a, b) is a continental fragment, which was once a part of a crustal basement of the East Asian continental margin prior to the back-arc opening of the Japan Sea in the mid-Miocene (e.g., Isozaki et al. 2010, 2023). It consists mainly of Permo-Triassic granite-gneiss complexes with Jurassic granitic intrusions. The metamorphic lithologies of the Hida Belt are mainly of granitic gneiss, amphibolite, marble, calcareous gneiss, quartzofeldspathic gneiss, and minor pelitic gneiss (cf., Ehiro et al. 2016). The timing of the upper amphibolite- to granulite-facies regional metamorphism has been dated as ~260–230 Ma (e.g., Cho et al. 2021; Horie et al. 2018; Takahashi et al. 2018).

In the Hida Belt, a large amount of metacarbonate rocks occur accompanying gneissose rocks (Kano 1998). The protolith has been regarded to be continental platform carbonates (e.g., Isozaki 1996, 1997; Sohma and Kunugiza 1993). The sedimentary origin of the metacarbonate rocks is supported by their C–O–Sr isotope compositions (Harada et al. 2021b). Most of the metacarbonate rocks in the Hida Belt consist mainly of calcite (i.e., calcite marble) with a minor amount of clinopyroxene, quartz, and titanite, whereas dolomitic marble which consists mainly of Mg-rich calcite and dolomite is rare (e.g., Harada et al. 2021b; Kano 1998). The calcite–dolomite solvus thermometry from calcite–dolomite intergrowth in dolomitic marble gives a temperature of ~600 °C (Imai et al. 1977; Kano 1998).

3 Analytical methods

Micro Raman spectroscopic analyses were performed to characterize fluid inclusions. Unpolarized Raman spectra were obtained by a laser Raman spectrometer, the HORIBA Jobin Yvon LabRAM300 at Tohoku University, connected to a 1024×256-pixel charge-coupled device (CCD) detector. The measurements used a 488 nm solid-state laser with a confocal hole of 200 μm, a slit width of 100 μm. The laser was focused through an Olympus MPlan 100× objective lens (N.A. = 0.9). The laser output was 25 mW at the source and approximately 5.0 mW at the sample surface. The laser spot size was approximately 1 μm. Grating with 600 lines/mm and 1800 lines/mm was used for analyses. The spectral resolution is ~5 cm^{-1} for 600 lines/mm grating and ~2 cm^{-1} for 1800 lines/mm grating. The pixel resolution of this Raman spectrometer when using a grating of 600 lines/mm is 5.5 cm^{-1}/pixel and 4.1 cm^{-1}/pixel at about 1000 cm^{-1} and 3650 cm^{-1}, respectively, and the resolution when using a grating of 1800 lines/mm is 1.8 cm^{-1}/pixel and 1.3 cm^{-1}/pixel at around 1000 cm^{-1} and 3650 cm^{-1}, respectively. Two accumulations of 10–120 s were collected for each spectrum. The calibration of the spectrometer was performed using a Si crystal and a diamond. The spectral baselines were corrected, and the spectra were fitted using the software package PeakFit v4.12 (SeaSolve Software Inc.).

4 Results

4.1 Sample description and petrography

The investigated dolomitic marble samples were collected from an outcrop along the Takahara River, Kamioka area, Gifu Prefecture (Fig. 1a, b). Although the dolomitic marble occurs surrounded by gneissose rocks and leucogranite, the contact between dolomitic marble and surrounding lithologies cannot be observed in the field. The dark-colored partially serpentinized olivine occurs as layers with a variety of widths (up to several tens of centimeters) in white carbonate minerals (Fig. 1c, d). The dolomitic marble exhibits variations in both the modal abundance and grain size of olivines.

The investigated dolomitic marble shows no remarkable foliation and commonly shows granoblastic texture. It consists mainly of Mg-rich calcite, dolomite, and olivine ($Fo_{\sim 89-93}$), with a small amount of tremolite, clinohumite, and phlogopite along with trace apatite (Fig. 2a). Carbonate minerals (calcite and dolomite) occur in a wide range of sizes (up to ~3 mm). The major carbonate minerals of the olivine-rich layer and carbonate-rich part are calcite and dolomite, respectively. Abundant tiny rectangular dolomite crystals were observed in calcite, suggesting the exsolution of dolomite from calcite. Olivine occurs as granular-shaped crystals with a wide range in size (up to ~3 mm). Almost all olivine crystals have partly or completely suffered serpentinization, forming serpentine, brucite, and magnetite (Fig. 2b). Olivine contains calcite, dolomite, and abundant fluid inclusions (Fig. 2c, d). Mesh texture after olivine is commonly observed. Raman

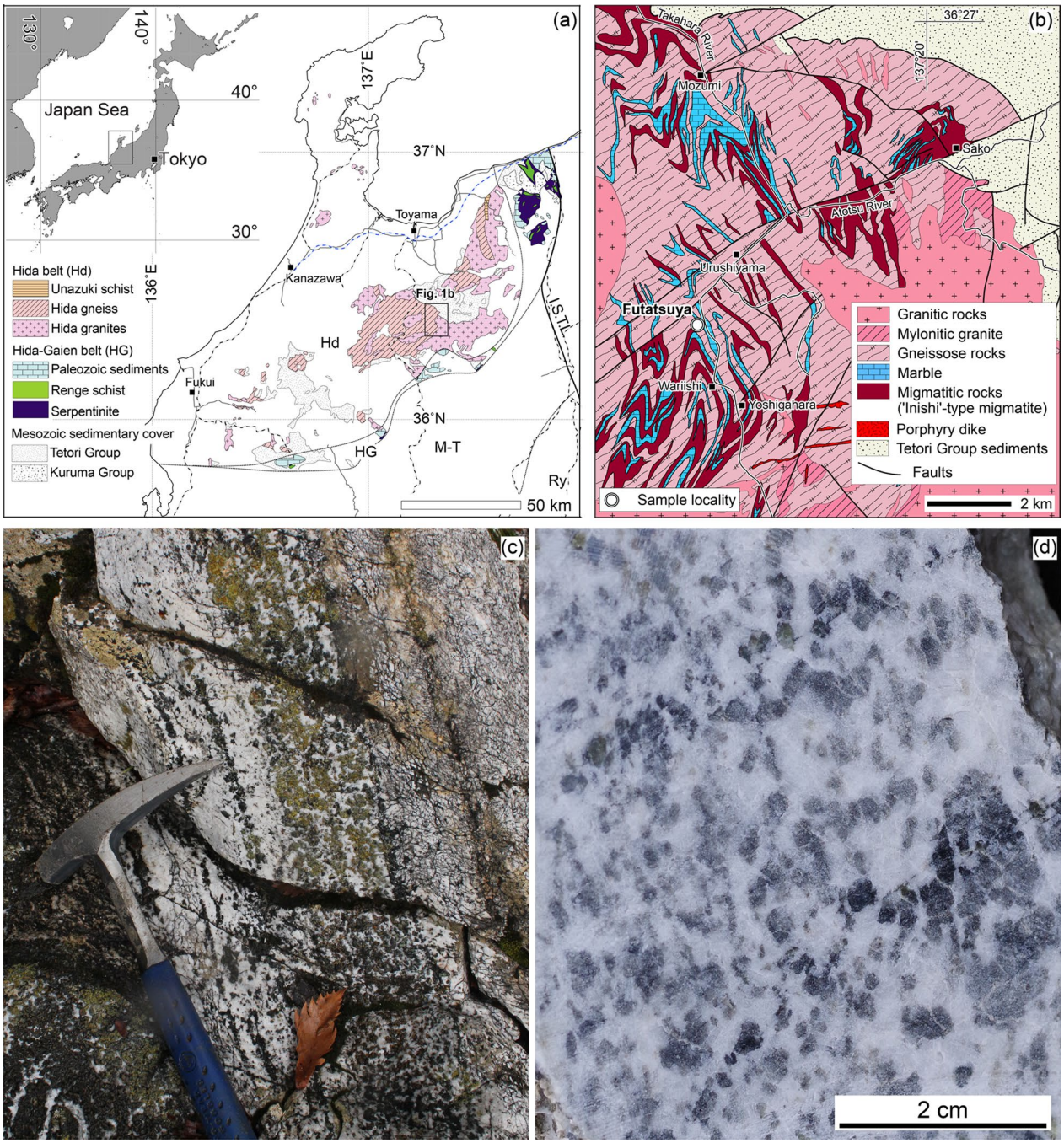

Fig. 1 Geological maps (**a**, **b**) and photographs of investigated dolomitic marble (**c**, **d**). **a** Simplified geological map of the Hokuriku region, showing locations of the Kamioka area (modified after Harada et al. 2021a,b). Hd, Hida Belt; HG, Hida-Gaien Belt; I.S.T.L., Itoigawa–Shizuoka Tectonic Line; M–T, Mino–Tamba Belt; Ry, Ryoke Belt. **b** A geological map of the Kamioka area, showing sample localities (modified after Harada et al. 2021a,b). **c** The field occurrence of the dolomitic marble (Kamioka area, the Hida Belt). **d** A sample slab of dolomitic marble. Black minerals are partially or completely serpentinized olivine

spectroscopic analyses show that the serpentines are lizardite and chrysotile.

4.2 Description of olivine-hosted fluid inclusions

Fluid inclusion analyses were performed on both thin sections and epoxy-mounted olivine crystals. Olivine

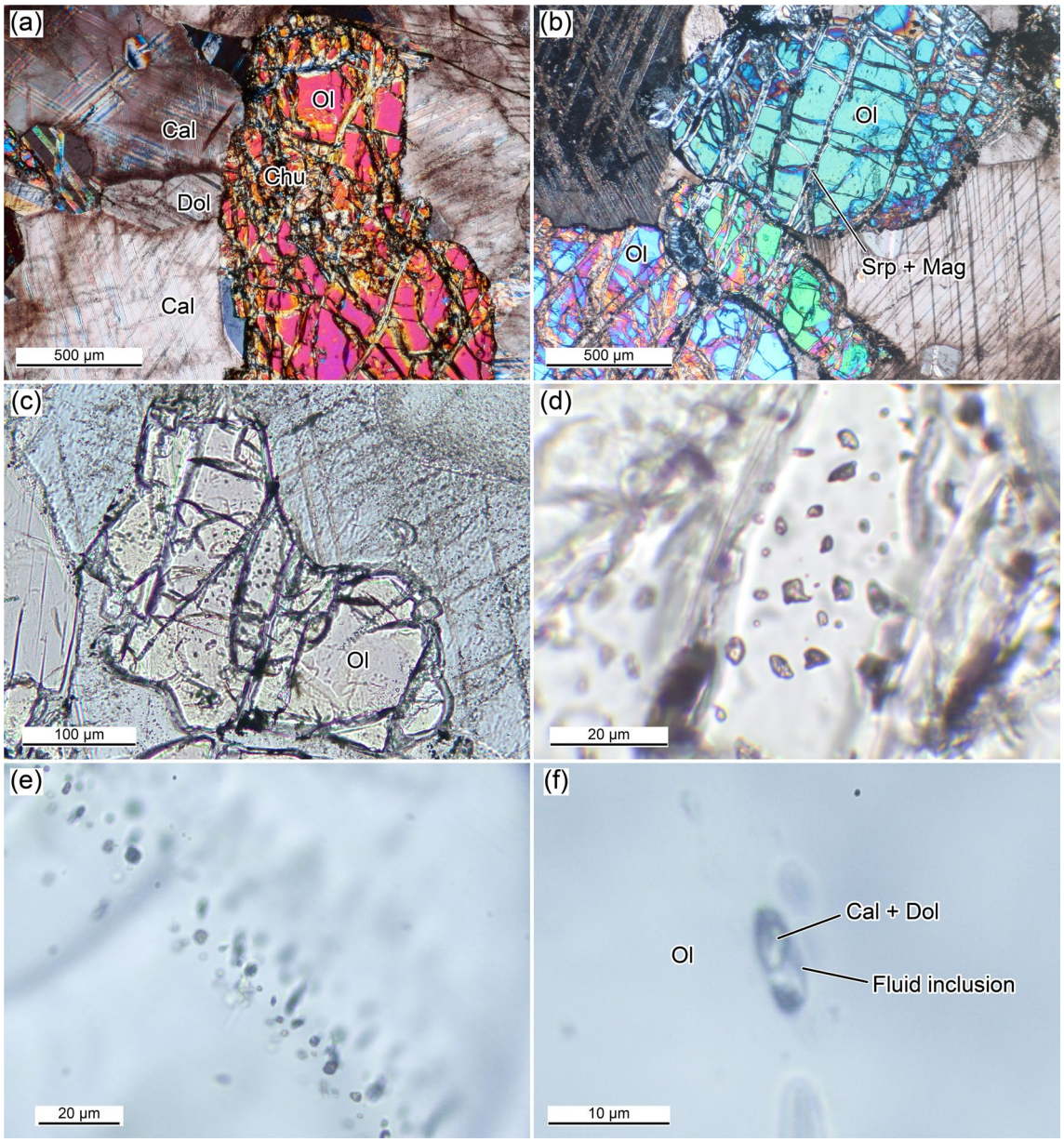

Fig. 2 Photomicrographs of investigated dolomitic marble. **a** Cross-polarized light (XPL) image of dolomitic marble. **b** XPL image of partially serpentinized olivine crystals in dolomitic marble. Serpentinization forms serpentine (lizardite) and magnetite. **c**, **d** Plane-polarized light (PPL) image of olivine crystals rich in fluid inclusions. **e** PPL image of olivine-hosted fluid inclusions with secondary nature. **f** PPL image of olivine-hosted primary fluid inclusion that contains calcite and dolomite. Mineral abbreviations follow Warr (2021)

grains were separated from sieved whole-rock powder using magnetic and heavy liquid techniques. Hand-picked olivine grains under a binocular microscope were mounted in 1-inch round epoxy resin discs. Olivine crystals in the investigated dolomitic marble often contain dark-colored fluid inclusions. The fluid inclusions vary from <1 to 10 μm in size and show irregular shape. There are two major types of olivine-hosted fluid inclusions, although discriminating between most inclusions is difficult. Primary fluid inclusions trapped during olivine growth occur as isolated inclusions, while secondary fluid inclusions, formed by fluid infiltration after olivine crystallization, occur as trails in olivine crystals (Fig. 2e). However, most inclusions are hard to discriminate as primary or secondary.

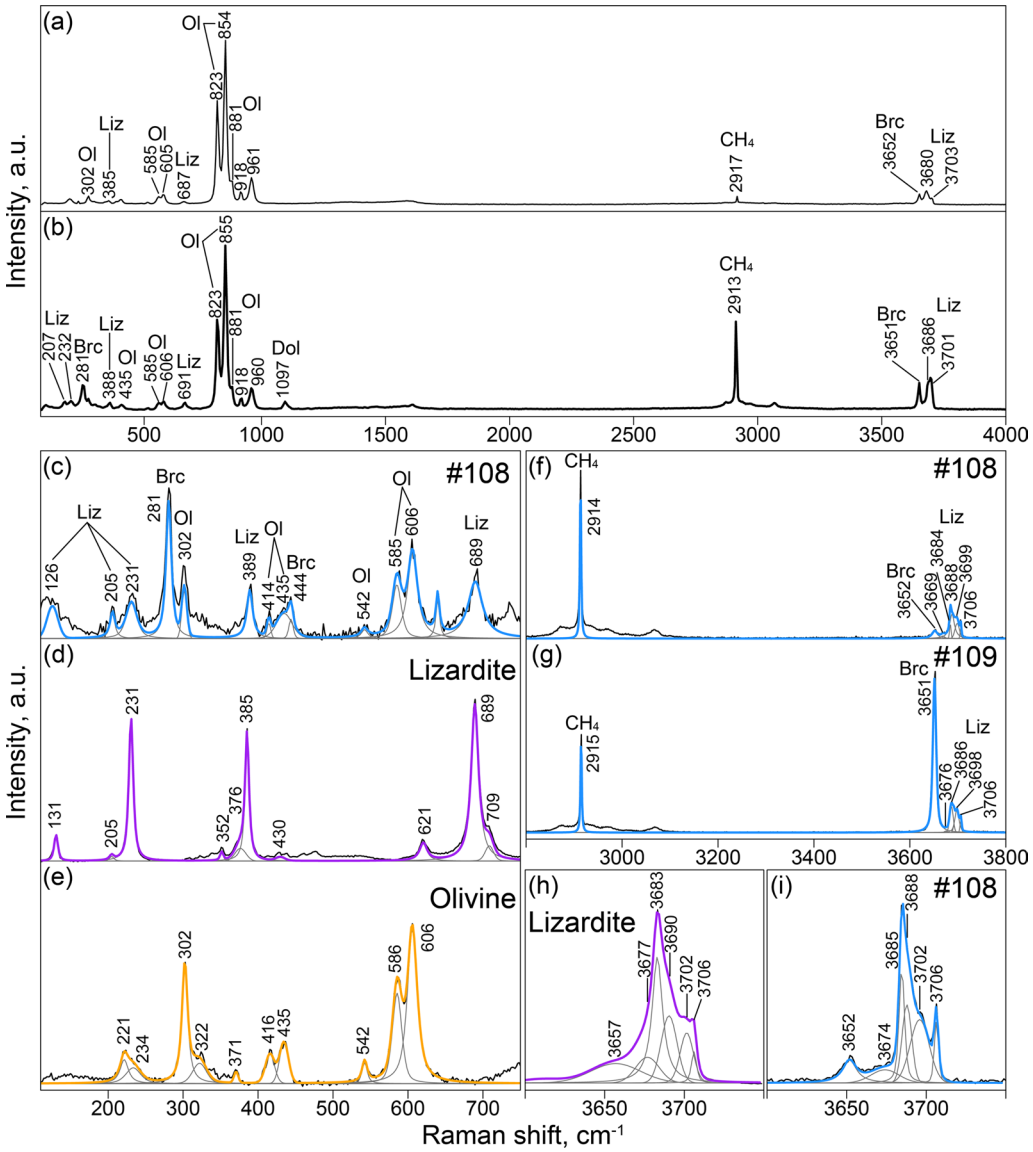

Fig. 3 Representative Raman spectra of olivine-hosted fluid inclusions in dolomitic marble from the Hida Belt. **a**, **b** Raman spectra of the olivine-hosted fluid inclusions. **c**–**e** Raman spectra of olivine-hosted fluid inclusion (**c**), lizardite in olivine rim (**d**), and host olivine (**e**) in low wavenumber spectral range (110–750 cm^{-1}). **f**, **g** Raman spectra of olivine-hosted fluid inclusion in high wavenumber spectral range (2800–3800 cm^{-1}). **h**, **i** Raman spectra of lizardite (**h**) and olivine-hosted fluid inclusion (**i**) in O–H stretching region (3600–3750 cm^{-1})

4.3 Raman spectroscopic analyses of olivine-hosted fluid inclusions

We performed Raman spectroscopic analyses for over 100 olivine-hosted fluid inclusions. Raman spectra of olivine-hosted fluid inclusions show a strong band at ~2913–2918 cm^{-1} (Figs. 3, 4, Additional file 1: Figure S1). This band can be assigned to the symmetric C–H stretching band of CH_4 vapor (e.g., Brunsgaard Hansen et al. 2001; Lu et al. 2007; Seitz et al. 1996). In addition to CH_4, several bands were observed in the high wavenumber region (~3600–3800 cm^{-1}) (Figs. 3,4, Additional file 1: Figure S1). These bands are originated from O–H stretching vibrations of hydrous minerals. On the low wavenumber region, Raman spectra of fluid inclusions show several bands in addition to the bands of the host olivine (Fig. 3c, e). The ~280 cm^{-1} and ~444 cm^{-1} bands (Fig. 3c) can be assigned to lattice vibrational modes of brucite (e.g., Dawson et al. 1973; Duffy et al. 1995; Zhu et al. 2019). Since brucite has a strong band at ~3650 cm^{-1} derived from O–H stretching vibration (e.g., Dawson et al. 1973; Duffy et al. 1995; Zhu et al. 2019), the ~3652 cm^{-1} band of

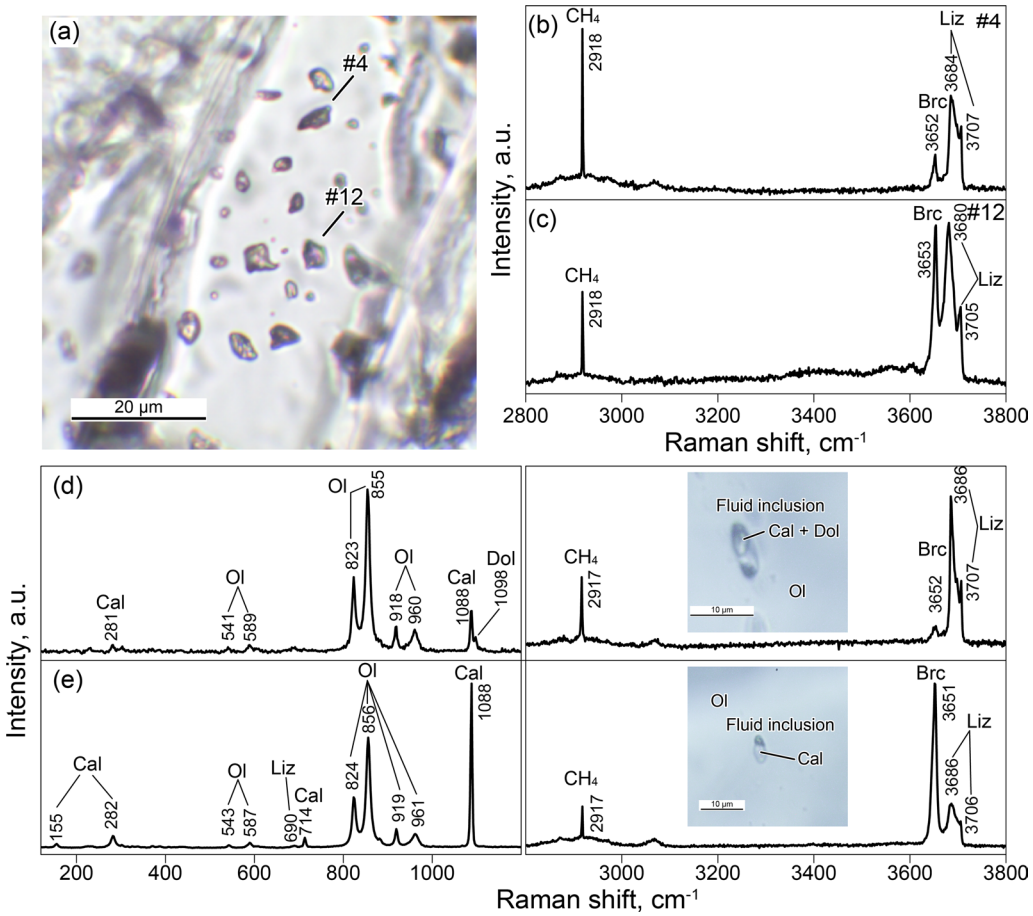

Fig. 4 Representative Raman spectra of olivine-hosted fluid inclusions. **a** PPL image of olivine-hosted fluid inclusions. **b**, **c** Raman spectra of the olivine-hosted fluid inclusions shown in (**b**). **d**, **e** Raman spectra of olivine-hosted fluid inclusions that contain carbonate minerals. Inclusion of **d** contains calcite and dolomite, and inclusions of **e** contains calcite

the fluid inclusion is attributed to brucite. In addition to olivine and brucite, Raman spectra of olivine-hosted fluid inclusions show ~130 cm^{-1}, 230 cm^{-1}, 390 cm^{-1}, and ~690 cm^{-1} bands (Fig. 3c). Similar peaks are also observed in matrix serpentine that occurs in rims and clacks of olivine crystals (Fig. 3d). We assigned these bands to serpentine minerals of lizardite or chrysotile (e.g., Auzende et al. 2004; Compagnoni et al. 2021; Groppo et al. 2006; Petriglieri et al. 2015; Rinaudo et al. 2003; Rooney et al. 2018; Tarling et al. 2018). Although lizardite and chrysotile have similar Raman spectra in the low wavenumber region, they can be distinguished by their O–H stretching bands in the high wavenumber spectral range (e.g., Auzende et al. 2004; Compagnoni et al. 2021; Petriglieri et al. 2015; Rooney et al. 2018; Tarling et al. 2018); lizardite has two major peaks while chrysotile has one peak with a slightly low wavenumber shoulder. Based on the presence of ~3685 cm^{-1} and ~3706 cm^{-1} peaks of the obtained spectrum (Fig. 3f, g, i), we considered that the serpentine in olivine-hosted fluid inclusions is lizardite. Raman spectrum of lizardite in high wavenumber spectral range consists of multiple bands (e.g., Auzende et al. 2004; Compagnoni et al. 2021). Compagnoni et al. (2021) obtained Raman spectra of lizardite under three different crystal orientations and deconvolved the O–H stretching region of lizardite into six bands. They reported that lizardite shows different Raman spectra and intensities for each orientation. Since we analyzed lizardite in fluid inclusions, it is difficult to perform a deconvolution that is completely consistent with the literature. Therefore, as previous studies have shown (Auzende et al. 2004; Petriglieri et al. 2015; Rooney et al. 2018; Tarling et al. 2018), we regarded that the Raman spectrum of lizardite in the O–H stretching region is characterized by two intense peaks at ~3680 cm^{-1} and >~3700 cm^{-1} (Fig. 3i). Although lizardite has a band of ~3650 cm^{-1}, it is not strong (Fig. 3h; Compagnoni et al. 2021; Rooney et al. 2018; Tarling et al. 2018). Hence, the intense peak

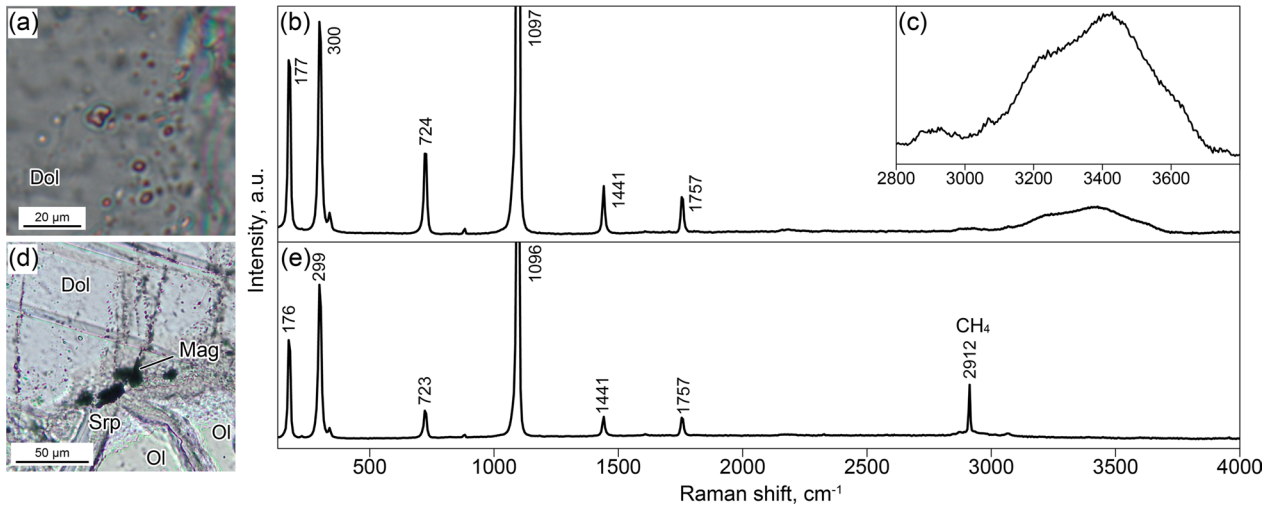

Fig. 5 Photomicrographs and representative Raman spectra of fluid inclusions in carbonate minerals. **a** PPL image of fluid inclusions in dolomite. **b** Raman spectrum of fluid inclusion in dolomite. Raman spectra of most fluid inclusions in calcite and dolomite show a broad band from around 2700–3800 cm^{-1}, which originates from O–H stretching modes of liquid water. **c** Enlarged view of O–H stretching region in the Raman spectrum of (**b**). PPL image (**d**) and Raman spectrum (**e**) of dolomite-hosted fluid inclusions that propagate from the serpentinized rim of olivine crystal

at ~3650 cm^{-1} can be considered to be that of brucite. Based on the above consideration, this study treats the Raman spectra of olivine-hosted fluid inclusions in the high wavenumber region as follows: The presence of brucite is characterized by the strong ~3650 cm^{-1} band, while other bands is derived from lizardite. Lizardite is characterized by two intense peaks at ~3680 cm^{-1} and >~3700 cm^{-1}. The CO_2, H_2O, and H_2 were not detected from investigated olivine-hosted fluid inclusions. The inclusion assemblage that contains CH_4, lizardite, and brucite was ubiquitously observed in investigated olivine-hosted fluid inclusions. In addition to the described inclusion assemblage, some primary fluid inclusions also contained carbonate minerals (Figs. 2f, 4d, e). Carbonate minerals in fluid inclusions show ~155 cm^{-1}, ~281 cm^{-1}, and ~714 cm^{-1} bands with a strong ~1088 cm^{-1} band (Fig. 4d, e) and are considered to be calcite. The peak position of the strong band of investigated carbonate mineral (~1088 cm^{-1}) was slightly higher than that of calcite in the literature (~1085 cm^{-1}: e.g., Bischoff et al. 1985; Dufresne et al. 2018; Gillet et al. 1993). The slight upshift of the band has been reported from Mg-calcite (e.g., Bischoff et al. 1985; Borromeo et al. 2017; Burke 2001), and the observed bands can be attributed to Mg-calcite. The ~1088 cm^{-1} band of Mg-calcite in fluid inclusions sometimes has a shoulder at a higher wavenumber side (~1098 cm^{-1}) (Fig. 4e), suggesting the presence of dolomite (e.g., Bischoff et al. 1985; Gillet et al. 1993). Since calcite and dolomite also occur as inclusion minerals in the olivine, carbonate minerals in fluid inclusions are considered an accidentally trapped mineral during host olivine growth.

4.4 Fluid inclusions in carbonate minerals

Calcite and dolomite also contained fluid inclusions (Fig. 5a, d). Raman spectra of most fluid inclusions in calcite and dolomite show a broad band from around 2700–3800 cm^{-1} (Fig. 5b, c), which is attributed to O–H stretching modes of liquid water (e.g., Walrafen 1964). Secondary fluid inclusions that propagate from the serpentinized rim of olivine crystals were rare and contained CH_4 (Fig. 5d, e). Note that these secondary CH_4 fluid inclusions in carbonate minerals lack H_2O.

5 Discussion

5.1 Origin of CH_4-bearing olivine-hosted fluid inclusions

Raman spectroscopic analysis of olivine-hosted fluid inclusions in dolomitic marble found the presence of CH_4, lizardite, and brucite (Figs. 3, 4, Additional file 1: Figure S1). The presence of serpentine and brucite in fluid inclusions is robust evidence that serpentinization occurred within olivine-hosted fluid inclusions as the result of the reaction between trapped fluid and host olivine crystals (Fig. 6). Therefore, it is reasonable to consider that the CH_4 was produced via the reduction of CO_2 by H_2 that originated from internal serpentinization within fluid inclusions (Grozeva et al. 2020; Klein et al. 2019; Miura et al. 2011; Zhang et al. 2021, 2022).

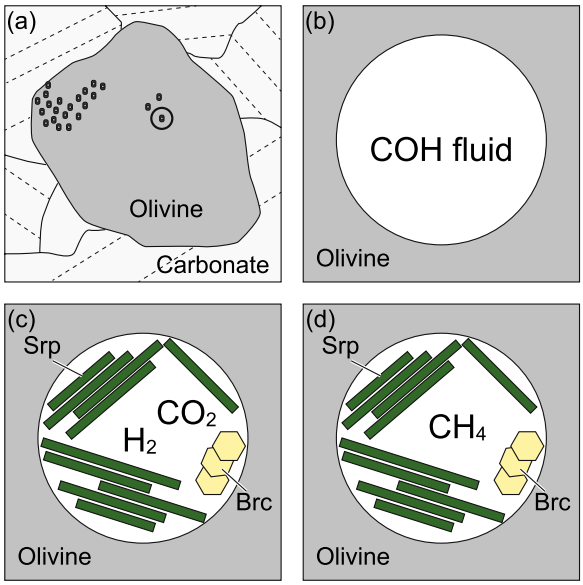

Fig. 6 Schematic diagram illustrating a model of serpentinization and accompanying CH_4 generation within olivine-hosted fluid inclusions. **a** Petrography of olivine-bearing dolomitic marble. **b** Olivine-hosted fluid inclusions originally contained H_2O and CO_2 (COH fluid) when they were trapped. **c** The decrease in temperature during the early stages of exhumation causes serpentinization of host olivine by trapped fluid and H_2 generation. **d** Generated H_2 reduced CO_2 and formed CH_4

Based on the observation, we postulate that olivine-hosted fluid inclusions originally contained H_2O and CO_2 (COH fluid) when they were trapped. As temperatures decreased upon exhumation, the trapped fluid caused serpentinization of the host olivine crystal and formed lizardite and brucite as step-daughter minerals. The serpentinization reaction generated H_2, and then the H_2 reduced CO_2 and formed CH_4. The origin of CO_2 in the trapped fluid can be attributed to metamorphic decarbonation and/or carbonate dissolution. The entrapment of primary fluid inclusions occurred during olivine growth in the upper-amphibolite to granulite facies peak metamorphic conditions of the Hida Belt. Since the formation of serpentine in fluid inclusions occurred after the fluid entrapment, the secondary fluid inclusions must have been trapped at conditions under which olivine is stable in the presence of H_2O. In other words, the fluid entrapment occurred prior to the matrix serpentinization of the host olivine crystal. Therefore, we can rule out the possibility that the CH_4 was derived from matrix serpentinization and was present in the fluid when it was trapped.

Although typical serpentinization reactions accompany the oxidation of iron and form magnetite, resulting in H_2 generation, the mineral inclusion assemblage of investigated olivine crystals lacks magnetite (Figs. 3, 4). However, there is a possibility that nanometer-sized magnetite crystals that cannot be detected by Raman spectroscopic analyses may be present in inclusions. Even if not, magnetite formation is not essential in H_2 production during serpentinization. Serpentine can accommodate a significant amount of ferric iron (Fe^{3+}) (e.g., Andreani et al. 2013; Fuchs et al. 1998; Klein et al. 2009; O'Hanley and Dyar 1993). Serpentine produced by the hydration of magnesium (Mg)-rich olivine contains Fe with a high $Fe^{3+}/(Fe^{3+}+Fe^{2+})$ ratio (Klein et al. 2013). The mineral assemblage formed by serpentinization depends on conditions such as temperature and water to rock ratio; magnetite may not be produced by the serpentinization of Fe-bearing olivine (Klein et al. 2013). In that case, the Fe^{3+} in serpentine contributes to the H_2 generation (e.g., Andreani et al. 2013; Klein et al. 2013; Marcaillou et al. 2011; Seyfried et al. 2007). Therefore, the absence of magnetite does not exclude the possibility of H_2-generation via serpentinization within fluid inclusions.

Secondary fluid inclusions in carbonate minerals that propagate from serpentine contained CH_4 and lacked H_2O. In contrast, the ubiquitous occurrence of hydrous minerals like serpentine and brucite in olivine-hosted fluid inclusions indicates that the inclusions initially contained H_2O. The contrast regarding the presence of water in fluid inclusions in olivine and carbonate minerals may reflect differences in the original fluid composition. Since CH_4 secondary fluid inclusions in calcite and dolomite propagate from serpentine, the origin of CH_4 in carbonate minerals can be attributed to the matrix serpentinization of olivine crystals, which formed serpentine minerals of olivine rim and clacks. Therefore, the entrapment timing of CH_4-bearing fluid inclusions hosted in olivine and carbonate minerals would have been different: Olivine-hosted fluid inclusions were trapped prior to the matrix serpentinization, whereas CH_4 secondary fluid inclusions in calcite and dolomite were formed during or after the serpentinization. Raman spectra of most of the fluid inclusions in calcite and dolomite show the presence of liquid H_2O. If these inclusions were formed during regional metamorphism, metamorphic fluid would not have contained CH_4. Fluid inclusions in carbonate minerals may support the abiotic CH_4 generation within olivine-hosted fluid inclusions. The possibility that the CH_4 in olivine-hosted fluid inclusions is of biological origin cannot be completely ruled out without measuring the carbon isotope compositions of the CH_4. However, the presence of H_2O-rich fluid inclusions in carbonate minerals and the mineralogy of olivine-hosted fluid inclusions indicate that the abiotic synthesis during internal serpentinization within fluid inclusions is a plausible origin of CH_4 in olivine-hosted fluid inclusions of dolomitic marble.

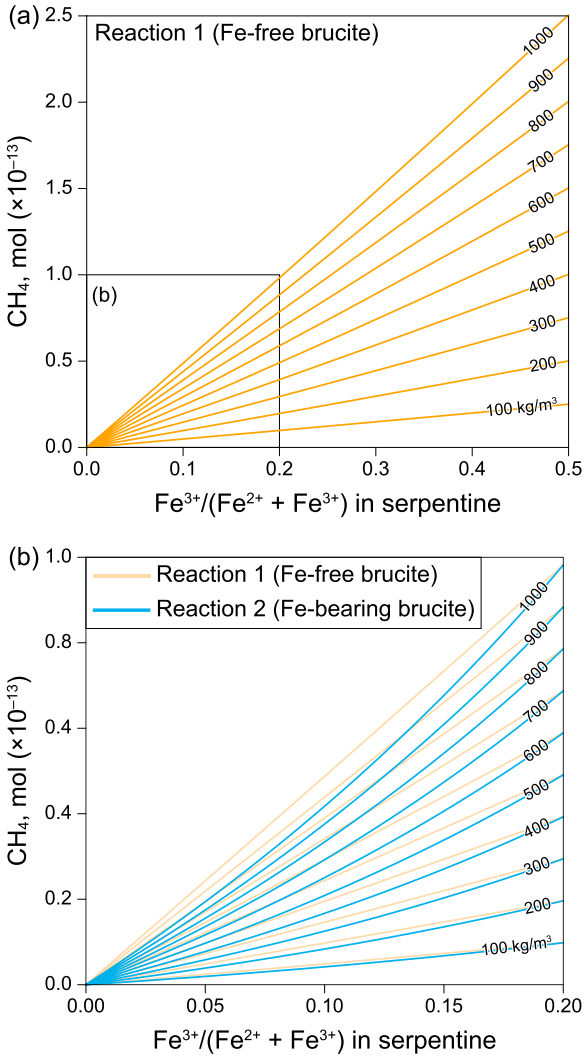

Fig. 7 The estimation of the amount of CH_4 produced within olivine-hosted fluid inclusions. Assuming spherical fluid inclusions with a diameter of 10 μm, the amount of CH_4 that could be produced by serpentinization without magnetite formation is calculated. The results of two simple reactions are shown; produced brucite is **a** Fe-free brucite and **b** Fe-bearing brucite. The number on the lines shows the assumed density of H_2O (100–1000 kg/m^3)

Assuming spherical fluid inclusions with a diameter of 10 μm, we estimated the amount of CH_4 that could be produced by the serpentinization without magnetite formation as a function of Fe^{3+} content in serpentine (Fig. 7). Two simple reactions were considered, one in which the product brucite is a pure Mg end-member (Reaction 1) and one in which the product brucite contains Fe (Reaction 2).

$$a\underset{\text{Olivine}}{\left(\mathrm{Mg}_{0.9},\mathrm{Fe}_{0.1}\right)_2\mathrm{SiO_4}} + b\mathrm{H_2O} \rightarrow c\underset{\text{Serpentine}}{\left(\mathrm{Mg}_x,\mathrm{Fe}^{2+}_y,\mathrm{Fe}^{3+}_z\right)\left(\mathrm{Fe}^{3+}_v,\mathrm{Si}_w\right)_2\mathrm{O_5(OH)_4}} + d\underset{\text{Brucite}}{\mathrm{Mg(OH)_2}} + e\mathrm{H_2}. \quad (1)$$

$$a\underset{\text{Olivine}}{\left(\mathrm{Mg}_{0.9},\mathrm{Fe}_{0.1}\right)_2\mathrm{SiO_4}} + b\mathrm{H_2O} \rightarrow c\underset{\text{Serpentine}}{\left(\mathrm{Mg}_x,\mathrm{Fe}^{2+}_y,\mathrm{Fe}^{3+}_z\right)\left(\mathrm{Fe}^{3+}_v,\mathrm{Si}_w\right)_2\mathrm{O_5(OH)_4}} + d\underset{\text{Brucite}}{\left(\mathrm{Mg}_s,\mathrm{Fe}_t\right)(\mathrm{OH})_2} + e\mathrm{H_2}. \quad (2)$$

For simplicity, the following assumptions were made. (1) Generated H_2 is not lost by diffusion. (2) Trapped fluid initially contains H_2O and CO_2, and the amount of CO_2 is sufficient to react with the generated H_2. (3) Among the products, only serpentine contains Fe^{3+}. Since we regard cronstedtite $[(Fe^{2+}{}_2Fe^{3+})_3(Fe^{3+}Si)_2O_5(OH)_4]$ as the Fe^{3+} end-member of serpentine (Evans 2008), the $Fe^{3+}/(Fe^{2+}+Fe^{3+})$ ratio of serpentine is up to 0.5. The serpentine formed by the serpentinization of Fo_{90} olivine has a $Fe^{3+}/(Fe^{2+}+Fe^{3+})$ ratio up to ~0.35 (Klein et al. 2013). Assuming the density of trapped H_2O is 1000 kg/m^3, each fluid inclusion has the potential to produce a maximum of $\sim 1.7\times10^{-13}$ mol CH_4. This CH_4 amount is comparable to the CH_4 content of olivine-hosted fluid inclusions in peridotite and gabbroic rocks (8.4×10^{-14} to 1.2×10^{-11} mol CH_4: Klein et al. 2019). Although the actual serpentinization reaction would be more complex, and this is a maximum estimation, it suggests the effective production of CH_4 in olivine-hosted fluid inclusions in dolomitic marble.

5.2 Implications for abiotic CH_4 synthesis during serpentinization

What is the significance of CH_4 synthesis in olivine-hosted fluid inclusions? Thermodynamic calculations show that serpentinization involving a small volume of fluid results in high H_2 concentration in fluids because the generated H_2 is less diluted (Klein et al. 2013). Olivine-hosted fluid inclusions can achieve a high H_2 concentration during serpentinization because the volume of trapped fluid is much smaller than the volume of the host olivine crystal. In addition, the infiltration of external fluids would not occur during serpentinization due to the isolated nature of the fluid inclusions within the olivine. This condition would be suitable for the reduction of CO_2 and production of CH_4. Experimental studies suggest that there are substantial kinetic barriers inhibiting abiotic CH_4 synthesis from the reduction of CO_2 unless certain catalysts, such as

FeNi alloys and chromite, are present (e.g., Foustoukos and Seyfried 2004; Horita and Berndt 1999; Klein and McCollom 2013; Lazar et al. 2012; McCollom 2016; McCollom and Seewald 2001); longer reaction times may be necessary to produce a significant amount of abiotic CH_4. However, fluid inclusions can retain high H_2 concentrations over much longer timescales than experimental studies. Therefore, internal serpentinization within fluid inclusions can be an effective pathway of abiotic CH_4 synthesis in the geological process.

High concentrations of geologically sourced hydrogen and hydrocarbon can have an impact on the Earth's biological activities. The microbial habitat extends to beneath Earth's surface, and Earth's subsurface biosphere, which has a large biomass (Magnabosco et al. 2018), relies for metabolisms on H_2 and CH_4 produced by fluid-rock interactions (e.g., Colman et al. 2017; Templeton and Caro 2023). In fact, some subsurface microbial communities would use serpentinite-derived H_2 and CH_4 (e.g., Schrenk et al. 2013). Recently, Vitale Brovarone et al. (2020) found that serpentinization generates reduced fluids, including H_2, CH_4, H_2S, and NH_3, and they suggested that these fluids may supply to the subsurface biosphere in the forearc region. In this study, we proposed the abiotic CH_4 synthesis in olivine-hosted fluid inclusions of dolomitic marble. The presence of microorganisms with anaerobic methane oxidation has been reported from granitic rocks as well as basalts and serpentinites (e.g., Ino et al. 2016; Kraus et al. 2021; Lever et al. 2013; Nothaft et al. 2021). If the olivine-hosted fluid is released, dolomitic marble may have the potential to provide abiotic CH_4 to the subsurface biosphere in the continental crust.

Abiotic CH_4 synthesis through internal serpentinization within olivine-hosted fluid inclusions has been widely recognized in mafic and ultramafic rocks (Grozeva et al. 2020; Klein et al. 2019; Miura et al. 2011; Zhang et al. 2021, 2022). This study provides the first finding of CH_4-bearing olivine-hosted fluid inclusions in metacarbonate rocks with sedimentary origin. We propose that serpentinization within olivine-hosted fluid inclusions is a ubiquitous process in olivine-bearing lithologies, not only in ultramafic rocks. Furthermore, since olivine-bearing dolomitic marbles occur in various orogenic belts with a wide range of metamorphic conditions (e.g., Kato et al. 1997; Liu et al. 2006; Ogasawara et al. 2000; Otsuji et al. 2013; Satish-Kumar et al. 2010; Yoshida et al. 2021), and even in contact metamorphic aureoles (e.g., Cook and Bowman 2000; Ferry et al. 2002; Holness 1997; Rice 1977), the dolomitic marble might have the potential to be the key lithology for the synthesis and storage of abiotic CH_4 in the continental crust and orogenic belts. In addition, the CH_4 in olivine-hosted fluid inclusions can be released by the weathering of exhumed dolomitic marble, and it might affect the atmospheric CH_4. To further our understanding of the contributions to the impact of abiotic CH_4 storage in the solid Earth, quantitative estimation of CH_4 production is still required.

Supplementary Information

The online version contains supplementary material available at https://doi.org/10.1186/s40645-024-00609-y.

Additional file 1: Figure S1. Representative Raman spectra of olivine-hosted fluid inclusions in high wavenumber spectral range (2800–3800 cm^{-1}).

Acknowledgements
We appreciate Yoshihide Ogasawara for donating a micro-Raman facility and dolomitic marble samples to CNEAS. We extend our appreciation to Tan Furukawa and Isamu Morita for their field assistance. We thank Maureen Feineman for her constructive feedback. We are grateful for constructive comments from two anonymous reviewers and thoughtful editorial handling by Madhusoodhan Satish-Kumar.

Author contributions
HH devised the project, conducted the analysis, and drafted the manuscript. TT supervised the project and contributed to the writing of the manuscript. All authors read and approved the final manuscript.

Funding
This research was supported by the Graduate School of Science and Center for Northeast Asian Studies, Tohoku University, in part by grants from the MEXT/JSPS KAKENHI JP22J21064 to HH, JP21H01174 to TT, ERI JURP 2021-B-01 in Earthquake Research Institute, the University of Tokyo, and the International Joint Graduate Program in Earth and Environmental Sciences (GP-EES) of Tohoku University.

Availability of data and materials
All data generated or analyzed during this study are included in this published article.

Declarations

Competing interests
The authors declare that they have no competing interest.

Received: 7 August 2023 Accepted: 2 February 2024
Published online: 12 February 2024

References

Andreani M, Muñoz M, Marcaillou C, Delacour A (2013) µXANES study of iron redox state in serpentine during oceanic serpentinization. Lithos 178:70–83. https://doi.org/10.1016/j.lithos.2013.04.008

Auzende AL, Daniel I, Reynard B, Lemaire C, Guyot F (2004) High-pressure behaviour of serpentine minerals: a Raman spectroscopic study. Phys Chem Miner 31:269–277. https://doi.org/10.1007/s00269-004-0384-0

Bischoff WD, Sharma SK, MacKenzie FT (1985) Carbonate ion disorder in synthetic and biogenic magnesian calcites: a Raman spectral study. Am Mineral 70:581–589

Borromeo L, Zimmermann U, Andò S, Coletti G, Bersani D, Basso D, Gentile P, Schulz B, Garzanti E (2017) Raman spectroscopy as a tool for magnesium

estimation in Mg-calcite. J Raman Spectrosc 48:983–992. https://doi.org/10.1002/jrs.5156
Boutier A, Vitale Brovarone A, Martinez I, Sissmann O, Mana S (2021) High-pressure serpentinization and abiotic methane formation in metaperidotite from the Appalachian subduction, northern Vermont. Lithos 396–397:106190. https://doi.org/10.1016/j.lithos.2021.106190
Brunsgaard Hansen S, Berg RW, Stenby EH (2001) Raman spectroscopic studies of methane–ethane mixtures as a function of pressure. Appl Spectrosc 55:745–749. https://doi.org/10.1366/0003702011952442
Burke EA (2001) Raman microspectrometry of fluid inclusions. Lithos 55:139–158. https://doi.org/10.1016/S0024-4937(00)00043-8
Cho DL, Lee TH, Takahashi Y, Kato T, Yi K, Lee S, Cheong ACS (2021) Zircon U-Pb geochronology and Hf isotope geochemistry of magmatic and metamorphic rocks from the Hida Belt, southwest Japan. Geosci Front 12:101145. https://doi.org/10.1016/j.gsf.2021.101145
Colman DR, Poudel S, Stamps BW, Boyd ES, Spear JR (2017) The deep, hot biosphere: twenty-five years of retrospection. Proc Natl Acad Sci USA 114:6895–6903. https://doi.org/10.1073/pnas.1701266114
Compagnoni R, Cossio R, Mellini M (2021) Raman anisotropy in serpentine minerals, with a caveat on identification. J Raman Spectrosc 52:1334–1345. https://doi.org/10.1002/jrs.6128
Cook SJ, Bowman JR (2000) Mineralogical evidence for fluid–rock interaction accompanying prograde contact metamorphism of siliceous dolomites: Alta Stock Aureole, Utah, USA. J Petrol 41:739–757. https://doi.org/10.1093/petrology/41.6.739
Dawson P, Hadfield CD, Wilkinson GR (1973) The polarized infra-red and Raman spectra of $Mg(OH)_2$ and $Ca(OH)_2$. J Phys Chem Solids 34:1217–1225. https://doi.org/10.1016/S0022-3697(73)80212-4
Duffy TS, Meade C, Fei Y, Mao HK, Hemley RJ (1995) High-pressure phase transition in brucite, $Mg(OH)_2$. Am Mineral 80:222–230. https://doi.org/10.2138/am-1995-3-404
Dufresne WJ, Rufledt CJ, Marshall CP (2018) Raman spectroscopy of the eight natural carbonate minerals of calcite structure. J Raman Spectrosc 49:1999–2007. https://doi.org/10.1002/jrs.5481
Ehiro M, Tsujimori T, Tsukada K, Nuramkhaan M (2016) Paleozoic basement and associated cover. In: Moreno T, Wallis S, Kojima T, Gibbons W (eds) The geology of Japan. Geological Society, London
Etiope G, Schoell M, Hosgörmez H (2011) Abiotic methane flux from the Chimaera seep and Tekirova ophiolites (Turkey): understanding gas exhalation from low temperature serpentinization and implications for Mars. Earth Planet Sci Lett 310:96–104. https://doi.org/10.1016/j.epsl.2011.08.001
Etiope G, Sherwood Lollar B (2013) Abiotic methane on Earth. Rev Geophys 51:276–299. https://doi.org/10.1002/rog.20011
Evans BW (2008) Control of the products of serpentinization by the $Fe^{2+}Mg_{-1}$ exchange potential of olivine and orthopyroxene. J Petrol 49:1873–1887. https://doi.org/10.1093/petrology/egn050
Evans BW (2010) Lizardite versus antigorite serpentinite: Magnetite, hydrogen, and life (?). Geology 38:879–882. https://doi.org/10.1130/G31158.1
Ferry JM, Wing BA, Penniston-Dorland SC, Rumble D (2002) The direction of fluid flow during contact metamorphism of siliceous carbonate rocks: new data for the Monzoni and Predazzo aureoles, northern Italy, and a global review. Contrib Mineral Petrol 142:679–699. https://doi.org/10.1007/s00410-001-0316-7
Foustoukos DI, Seyfried WE Jr (2004) Hydrocarbons in hydrothermal vent fluids: the role of chromium-bearing catalysts. Science 304:1002–1005. https://doi.org/10.1126/science.1096033
Fuchs Y, Linares J, Mellini M (1998) Mössbauer and infrared spectrometry of lizardite-*1T* from Monte Fico, Elba. Phys Chem Miner 26:111–115. https://doi.org/10.1007/s002690050167
Gillet P, Biellmann C, Reynard B, McMillan P (1993) Raman spectroscopic studies of carbonates part I: high-pressure and high-temperature behaviour of calcite, magnesite, dolomite and aragonite. Phys Chem Miner 20:1–18. https://doi.org/10.1007/BF00202245
Groppo C, Rinaudo C, Cairo S, Gastaldi D, Compagnoni R (2006) Micro-Raman spectroscopy for a quick and reliable identification of serpentine minerals from ultramafics. Eur J Mineral 18:319–329. https://doi.org/10.1127/0935-1221/2006/0018-0319
Grozeva NG, Klein F, Seewald JS, Sylva SP (2020) Chemical and isotopic analyses of hydrocarbon-bearing fluid inclusions in olivine-rich rocks. Philos Trans R Soc A 378:20180431. https://doi.org/10.1098/rsta.2018.0431
Harada H, Tsujimori T, Kon Y, Aoki S, Aoki K (2021a) Nature and timing of anatectic event of the Hida Belt (Japan): constraints from titanite geochemistry and U-Pb age of clinopyroxene-bearing leucogranite. Lithos 398–399:106256. https://doi.org/10.1016/j.lithos.2021.106256
Harada H, Tsujimori T, Kunugiza K, Yamashita K, Aoki S, Aoki K, Takayanagi H, Iryu Y (2021b) The $\delta^{13}C$–$\delta^{18}O$ variations in marble in the Hida Belt. Japan Isl Arc 30:e12389. https://doi.org/10.1111/iar.12389
Holness MB (1997) Fluid flow paths and mechanisms of fluid infiltration in carbonates during contact metamorphism: the Beinn an Dubhaich aureole, Skye. J Metamorph Geol 15:59–70. https://doi.org/10.1111/j.1525-1314.1997.00005.x
Horie K, Tsutsumi Y, Takehara M, Hidaka H (2018) Timing and duration of regional metamorphism in the Kagasawa and Unazuki areas, Hida metamorphic complex, southwest Japan. Chem Geol 484:148–167. https://doi.org/10.1016/j.chemgeo.2017.12.016
Horita J, Berndt ME (1999) Abiogenic methane formation and isotopic fractionation under hydrothermal conditions. Science 285:1055–1057. https://doi.org/10.1126/science.285.5430.1055
Imai N, Ogasawara Y, Wakabayashi N, Terao Y (1977) Carbonate rocks in the Hida Metamorphic Belts with special reference to the intergrowths of dolomite and the cementing magnesian calcite (Preliminary Report) Preliminary remarks to the petrology on the calcareous gneisses and metamorphic carbonate rocks in the Hida Metamorphic Belts, Central Japan. Bull Sci Eng Res Lab Waseda Univ 78:26–42 (**in Japanese with English abstract**)
Ino K, Konno U, Kouduka M, Hirota A, Togo YS, Fukuda A, Komatsu D, Tsunogai U, Tanabe AS, Yamamoto S, Iwatsuki T, Mizuno T, Ito K, Suzuki Y (2016) Deep microbial life in high-quality granitic groundwater from geochemically and geographically distinct underground boreholes. Environ Microbiol Rep 8:285–294. https://doi.org/10.1111/1758-2229.12379
Isozaki Y (1996) Anatomy and genesis of a subduction-related orogen: a new view of geotectonic subdivision and evolution of the Japanese Islands. Isl Arc 5:289–320. https://doi.org/10.1111/j.1440-1738.1996.tb00033.x
Isozaki Y (1997) Contrasting two types of orogen in Permo-Triassic Japan: accretionary versus collisional. Isl Arc 6:2–24. https://doi.org/10.1111/j.1440-1738.1997.tb00038.x
Isozaki Y, Aoki K, Nakama T, Yanai S (2010) New insight into a subduction-related orogen: a reappraisal of the geotectonic framework and evolution of the Japanese Islands. Gondwana Res 18:82–105. https://doi.org/10.1016/j.gr.2010.02.015
Isozaki Y, Sawaki Y, Iwano H, Hirata T, Kunugiza K (2023) Late Triassic A-type granite boulders in Lower Cretaceous conglomerate of the Hida belt, Japan: their origin and bearing on the Yamato tectonic line in Far East Asia. Isl Arc 32:e12475. https://doi.org/10.1111/iar.12475
Kano T (1998) Crystalline limestone in the Hida metamorphic complex, central Japan-Geological characteristics, mineral compositions, texture and mode of occurrences of dolomite. Shigen-Chishitsu 48:77–92. https://doi.org/10.11456/shigenchishitsu1992.48.77. (**in Japanese with English abstract**)
Kato T, Enami M, Zhai M (1997) Ultra-high-pressure (UHP) marble and eclogite in the Su-Lu UHP terrane, eastern China. J Metamorph Geol 15:169–182. https://doi.org/10.1111/j.1525-1314.1997.00013.x
Kelley DS, Karson JA, Fruh-Green GL, Yoerger DR, Shank TM, Butterfield DA, Hayes JM, Schrenk MO, Olson EJ, Proskurowski G, Jakuba M, Bradley A, Larson B, Ludwig K, Glickson D, Buckman K, Bradley AS, Brazelton WJ, Roe K, Elend MJ, Delacour A, Bernasconi SM, Lilley MD, Baross JA, Summons RE, Sylva SP (2005) A serpentinite-hosted ecosystem: the Lost City hydrothermal field. Science 307:1428–1434. https://doi.org/10.1126/science.1102556
Klein F, McCollom TM (2013) From serpentinization to carbonation: new insights from a CO_2 injection experiment. Earth Planet Sci Lett 379:137–145. https://doi.org/10.1016/j.epsl.2013.08.017
Klein F, Bach W, Jöns N, McCollom T, Moskowitz B, Berquó T (2009) Iron partitioning and hydrogen generation during serpentinization of abyssal peridotites from 15 N on the Mid-Atlantic Ridge. Geochim Cosmochim Acta 73:6868–6893. https://doi.org/10.1016/j.gca.2009.08.021
Klein F, Bach W, McCollom TM (2013) Compositional controls on hydrogen generation during serpentinization of ultramafic rocks. Lithos 178:55–69. https://doi.org/10.1016/j.lithos.2013.03.008

Klein F, Grozeva NG, Seewald JS (2019) Abiotic methane synthesis and serpentinization in olivine-hosted fluid inclusions. Proc Natl Acad Sci USA 116:17666–17672. https://doi.org/10.1073/pnas.1907871116

Kraus EA, Nothaft D, Stamps BW, Rempfert KR, Ellison ET, Matter JM, Templeton AS, Boyd ES, Spear JR (2021) Molecular evidence for an active microbial methane cycle in subsurface serpentinite-hosted groundwaters in the Samail Ophiolite, Oman. Appl Environ Microbiol 87:e02068-e2120. https://doi.org/10.1128/AEM.02068-20

Lazar C, McCollom TM, Manning CE (2012) Abiogenic methanogenesis during experimental komatiite serpentinization: implications for the evolution of the early Precambrian atmosphere. Chem Geol 326:102–112. https://doi.org/10.1016/j.chemgeo.2012.07.019

Lever MA, Rouxel O, Alt JC, Shimizu N, Ono S, Coggon RM, Shanks WC III, Lapham L, Elvert M, Prieto-Mollar X, Hinrichs KU, Inagaki F, Teske A (2013) Evidence for microbial carbon and sulfur cycling in deeply buried ridge flank basalt. Science 339:1305–1308. https://doi.org/10.1126/science.1229240

Liu FL, Gerdes A, Liou JG, Xue HM, Liang FH (2006) SHRIMP U-Pb zircon dating from Sulu-Dabie dolomitic marble, eastern China: constraints on prograde, ultrahigh-pressure and retrograde metamorphic ages. J Metamorph Geol 24:569–589. https://doi.org/10.1111/j.1525-1314.2006.00655.x

Lu W, Chou IM, Burruss RC, Song Y (2007) A unified equation for calculating methane vapor pressures in the CH_4–H_2O system with measured Raman shifts. Geochim Cosmochim Acta 71:3969–3978. https://doi.org/10.1016/j.gca.2007.06.004

Magnabosco C, Lin LH, Dong H, Bomberg M, Ghiorse W, Stan-Lotter H, Pedersen K, Kieft TL, van Heerden E, Onstott TC (2018) The biomass and biodiversity of the continental subsurface. Nat Geosci 11:707–717. https://doi.org/10.1038/s41561-018-0221-6

Marcaillou C, Munoz M, Vidal O, Parra T, Harfouche M (2011) Mineralogical evidence for H_2 degassing during serpentinization at 300 °C/300 bar. Earth Planet Sci Lett 303:281–290. https://doi.org/10.1016/j.epsl.2011.01.006

McCollom TM (2016) Abiotic methane formation during experimental serpentinization of olivine. Proc Natl Acad Sci USA 113:13965–13970. https://doi.org/10.1073/pnas.1611843113

McCollom TM, Bach W (2009) Thermodynamic constraints on hydrogen generation during serpentinization of ultramafic rocks. Geochim Cosmochim Acta 73:856–875. https://doi.org/10.1016/j.gca.2008.10.032

McCollom TM, Seewald JS (2001) A reassessment of the potential for reduction of dissolved CO_2 to hydrocarbons during serpentinization of olivine. Geochim Cosmochim Acta 65:3769–3778. https://doi.org/10.1016/S0016-7037(01)00655-X

Miller HM, Matter JM, Kelemen P, Ellison ET, Conrad ME, Fierer N, Ruchala T, Tominaga M, Templeton AS (2016) Modern water/rock reactions in Oman hyperalkaline peridotite aquifers and implications for microbial habitability. Geochim Cosmochim Acta 179:217–241. https://doi.org/10.1016/j.gca.2016.01.033

Miura M, Arai S, Mizukami T (2011) Raman spectroscopy of hydrous inclusions in olivine and orthopyroxene in ophiolitic harzburgite: implications for elementary processes in serpentinization. J Mineral Petrol Sci 106:91–96. https://doi.org/10.2465/jmps.101021d

Mottl MJ, Komor SC, Fryer P, Moyer CL (2003) Deep-slab fluids fuel extremophilic Archaea on a Mariana forearc serpentinite mud volcano: Ocean Drilling Program Leg 195. Geochem Geophys Geosyst 4:9009. https://doi.org/10.1029/2003GC000588

Nothaft DB, Templeton AS, Rhim JH, Wang DT, Labidi J, Miller HM, Boyd ES, Matter JM, Ono S, Young ED, Kopf SH, Kelemen PB, Conrad ME, Oman Drilling Project Science Team (2021) Geochemical, biological, and clumped isotopologue evidence for substantial microbial methane production under carbon limitation in serpentinites of the Samail Ophiolite, Oman. J Geophys Res Biogeosci 126:e2020JG006025. https://doi.org/10.1029/2020JG006025

Ogasawara Y, Ohta M, Fukasawa K, Katayama I, Maruyama S (2000) Diamond-bearing and diamond-free metacarbonate rocks from Kumdy-Kol in the Kokchetav Massif, northern Kazakhstan. Isl Arc 9:400–416. https://doi.org/10.1046/j.1440-1738.2000.00285.x

O'Hanley DS, Dyar MD (1993) The composition of lizardite *1T* and the formation of magnetite in serpentinites. Am Mineral 78:391–404

Ohara Y, Reagan MK, Fujikura K, Watanabe H, Michibayashi K, Ishii T, Stern RJ, Pujana I, Martinez F, Girard G, Ribeiro J, Brounce M, Komori N, Kino M (2012) A serpentinite-hosted ecosystem in the Southern Mariana Forearc. Proc Natl Acad Sci USA 109:2831–2835. https://doi.org/10.1073/pnas.1112005109

Otsuji N, Satish-Kumar M, Kamei A, Tsuchiya N, Kawakami T, Ishikawa M, Grantham GH (2013) Late-Tonian to early-Cryogenian apparent depositional ages for metacarbonate rocks from the Sør Rondane Mountains, East Antarctica. Precambrian Res 234:257–278. https://doi.org/10.1016/j.precamres.2012.10.016

Petriglieri JR, Salvioli-Mariani E, Mantovani L, Tribaudino M, Lottici PP, Laporte-Magoni C, Bersani D (2015) Micro-Raman mapping of the polymorphs of serpentine. J Raman Spectrosc 46:953–958. https://doi.org/10.1002/jrs.4695

Proskurowski G, Lilley MD, Seewald JS, Früh-Green GL, Olson EJ, Lupton JE, Sylva SP, Kelley DS (2008) Abiogenic hydrocarbon production at Lost City hydrothermal field. Science 319:604–607. https://doi.org/10.1126/science.1151194

Rice JM (1977) Contact metamorphism of impure dolomitic limestone in the Boulder aureole, Montana. Contrib Mineral Petrol 59:237–259. https://doi.org/10.1007/BF00374555

Rinaudo C, Gastaldi D, Belluso E (2003) Characterization of chrysotile, antigorite and lizardite by FT-Raman spectroscopy. Can Mineral 41:883–890. https://doi.org/10.2113/gscanmin.41.4.883

Rooney JS, Tarling MS, Smith SA, Gordon KC (2018) Submicron Raman spectroscopy mapping of serpentinite fault rocks. J Raman Spectrosc 49:279–286. https://doi.org/10.1002/jrs.5277

Satish-Kumar M, Hermann J, Miyamoto T, Osanai Y (2010) Fingerprinting a multistage metamorphic fluid–rock history: evidence from grain scale Sr, O and C isotopic and trace element variations in high-grade marbles from East Antarctica. Lithos 114:217–228. https://doi.org/10.1016/j.lithos.2009.08.010

Schrenk MO, Brazelton WJ, Lang SQ (2013) Serpentinization, carbon, and deep life. Rev Mineral Geochem 75:575–606. https://doi.org/10.2138/rmg.2013.75.18

Seitz JC, Pasteris JD, Chou IM (1996) Raman spectroscopic characterization of gas mixtures; II, quantitative composition and pressure determination of the CO_2-CH_4 system. Am J Sci 296:577–600. https://doi.org/10.2475/ajs.296.6.577

Seyfried WE Jr, Foustoukos DI, Fu Q (2007) Redox evolution and mass transfer during serpentinization: an experimental and theoretical study at 200 °C, 500 bar with implications for ultramafic-hosted hydrothermal systems at Mid-Ocean Ridges. Geochim Cosmochim Acta 71:3872–3886. https://doi.org/10.1016/j.gca.2007.05.015

Sohma T, Kunugiza K (1993) The formation of the Hida nappe and the tectonics of Mesozoic sediments: the tectonic evolution of the Hida region, Central Japan. Mem Geol Soc Japan 42:1–20 (**in Japanese with English abstract**)

Sleep NH, Meibom A, Fridriksson T, Coleman RG, Bird DK (2004) H_2-rich fluids from serpentinization: geochemical and biotic implications. Proc Natl Acad Sci USA 101:12818–12823. https://doi.org/10.1073/pnas.0405289101

Spránitz T, Padrón-Navarta JA, Szabó C, Szabó Á, Berkesi M (2022) Abiotic passive nitrogen and methane enrichment during exhumation of subducted rocks: primary multiphase fluid inclusions in high-pressure rocks from the Cabo Ortegal Complex, NW Spain. J Metamorph Geol 40:1291–1319. https://doi.org/10.1111/jmg.12666

Suda K, Ueno Y, Yoshizaki M, Nakamura H, Kurokawa K, Nishiyama E, Yoshino K, Hongoh Y, Kawachi K, Omori S, Yamada K, Yoshida N, Maruyama S (2014) Origin of methane in serpentinite-hosted hydrothermal systems: the CH_4–H_2–H_2O hydrogen isotope systematics of the Hakuba Happo hot spring. Earth Planet Sci Lett 386:112–125. https://doi.org/10.1016/j.epsl.2013.11.001

Takahashi Y, Cho DL, Mao J, Zhao X, Yi K (2018) SHRIMP U-Pb zircon ages of the Hida metamorphic and plutonic rocks, Japan: implications for late Paleozoic to Mesozoic tectonics around the Korean Peninsula. Isl Arc 27:e12220. https://doi.org/10.1111/iar.12220

Tao R, Zhang L, Tian M, Zhu J, Liu X, Liu J, Höfer HF, Stagno V, Fei Y (2018) Formation of abiotic hydrocarbon from reduction of carbonate in subduction zones: constraints from petrological observation and experimental simulation. Geochim Cosmochim Acta 239:390–408. https://doi.org/10.1016/j.gca.2018.08.008

Tarling MS, Rooney JS, Viti C, Smith SA, Gordon KC (2018) Distinguishing the Raman spectrum of polygonal serpentine. J Raman Spectrosc 49:1978–1984. https://doi.org/10.1002/jrs.5475

Templeton AS, Caro TA (2023) The rock-hosted biosphere. Annu Rev Earth Planet Sci 51:493–519. https://doi.org/10.1146/annurev-earth-031920-081957

Vitale Brovarone A, Sverjensky DA, Piccoli F, Ressico F, Giovannelli D, Daniel I (2020) Subduction hides high-pressure sources of energy that may feed the deep subsurface biosphere. Nat Commun 11:3880. https://doi.org/10.1038/s41467-020-17342-x

Walrafen GE (1964) Raman spectral studies of water structure. J Chem Phys 40:3249–3256. https://doi.org/10.1063/1.1724992

Wang C, Tao R, Walters JB, Höfer HE, Zhang L (2022) Favorable *P-T–f*O_2 conditions for abiotic CH_4 production in subducted oceanic crusts: a comparison between CH_4-bearing ultrahigh-and CO_2-bearing high-pressure eclogite. Geochim Cosmochim Acta 336:269–290. https://doi.org/10.1016/j.gca.2022.09.010

Warr LN (2021) IMA–CNMNC approved mineral symbols. Mineral Mag 85:291–320. https://doi.org/10.1180/mgm.2021.43

Yoshida S, Ishikawa A, Aoki S, Komiya T (2021) Occurrence and chemical composition of the Eoarchean carbonate rocks of the Nulliak supracrustal rocks in the Saglek Block of northeastern Labrador. Canada Isl Arc 30:e12381. https://doi.org/10.1111/iar.12381

Zhang L, Wang Q, Ding X, Li WC (2021) Diverse serpentinization and associated abiotic methanogenesis within multiple types of olivine-hosted fluid inclusions in orogenic peridotite from northern Tibet. Geochim Cosmochim Acta 296:1–17. https://doi.org/10.1016/j.gca.2020.12.016

Zhang L, Wang Q, Mikhailenko DS, Ding X, Li WC, Xian H (2022) Hydroxychloride-bearing fluid inclusions in ultramafic rocks from New Caledonia: implications for serpentinization in saline environments on earth and beyond. J Geophys Res Solid Earth 127:e2022JB024508. https://doi.org/10.1029/2022JB024508

Zhu X, Guo X, Smyth JR, Ye Y, Wang X, Liu D (2019) High-temperature vibrational spectra between $Mg(OH)_2$ and $Mg(OD)_2$: anharmonic contribution to thermodynamics and D/H fractionation for brucite. J Geophys Res Solid Earth 124:8267–8280. https://doi.org/10.1029/2019JB017934

Publisher's Note

Additional file 1. Supplementary figures
Figure S1

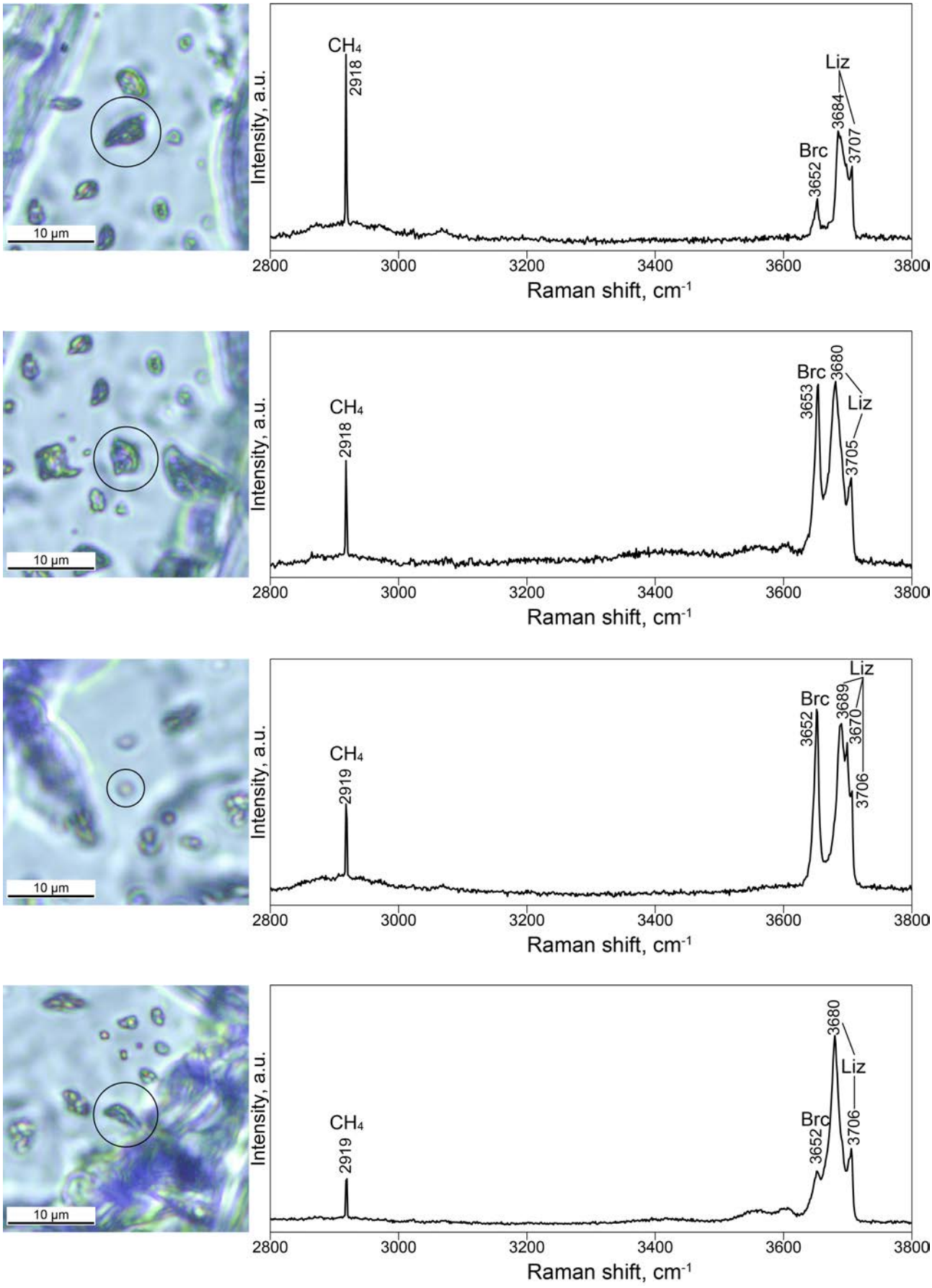

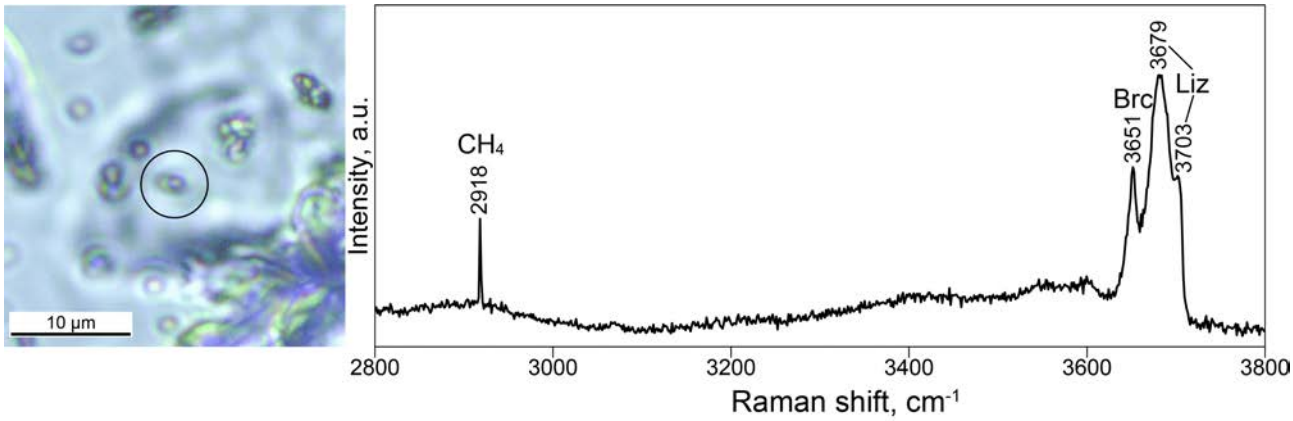
10 μm
CH4
2918
Intensity, a.u.
Brc
3651
3679
Liz
3703
2800
3000
3200
3400
3600
3800
Raman shift, cm-1

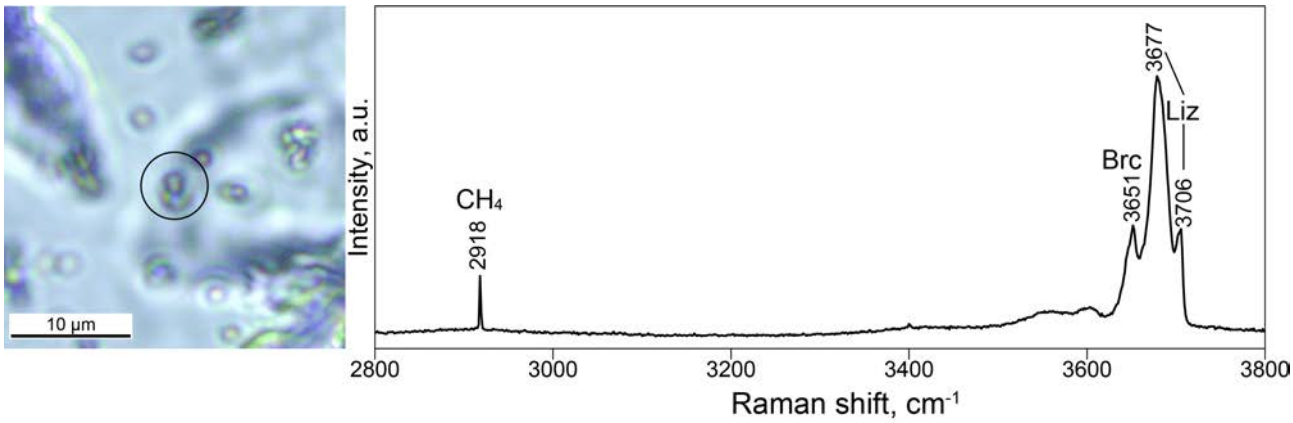
10 μm
CH4
2918
Intensity, a.u.
Brc
3651
3677
Liz
3706
2800
3000
3200
3400
3600
3800
Raman shift, cm-1

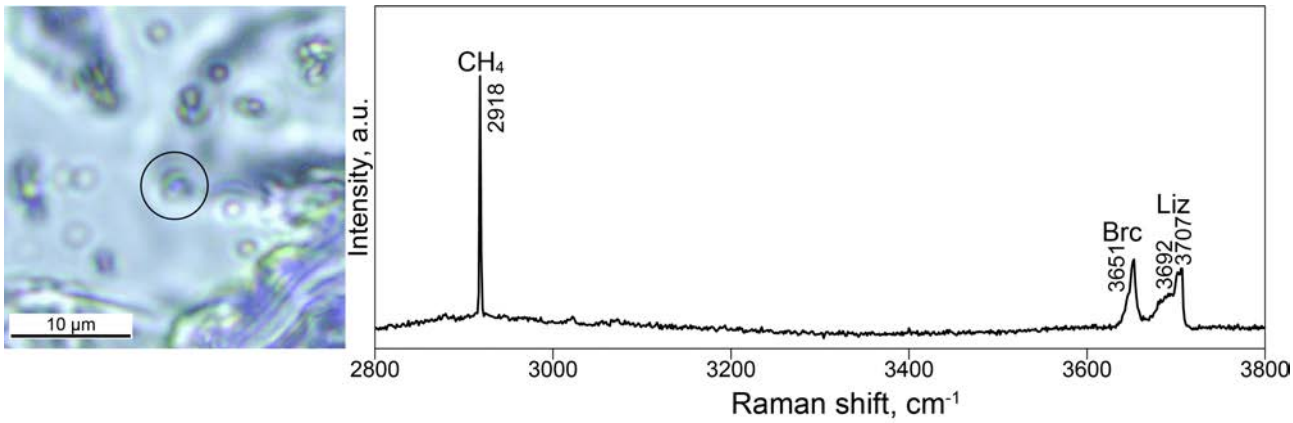
10 μm
CH4
2918
Intensity, a.u.
Brc
3651
Liz
3692
3707
2800
3000
3200
3400
3600
3800
Raman shift, cm-1

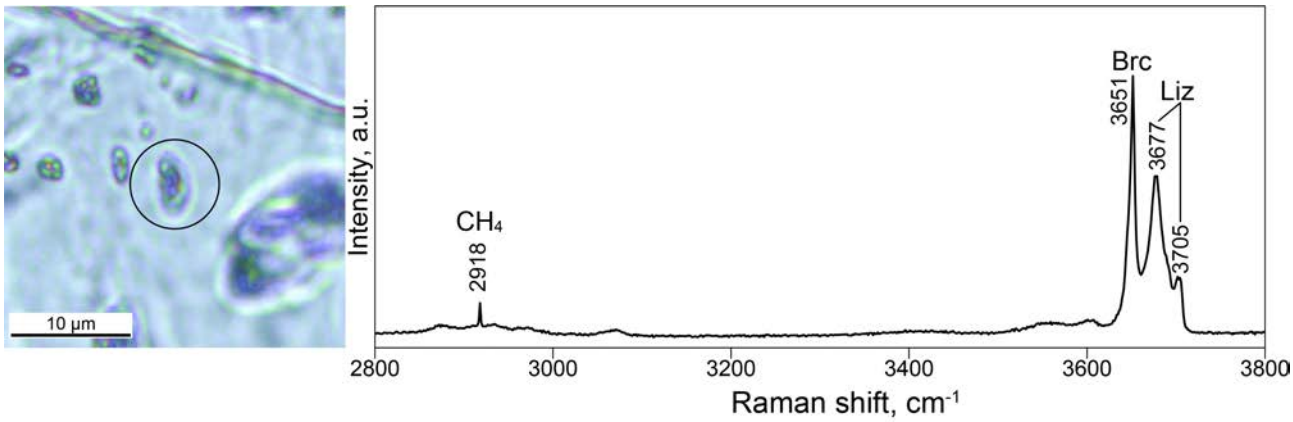
10 μm
CH4
2918
Intensity, a.u.
Brc
3651
Liz
3677
3705
2800
3000
3200
3400
3600
3800
Raman shift, cm-1

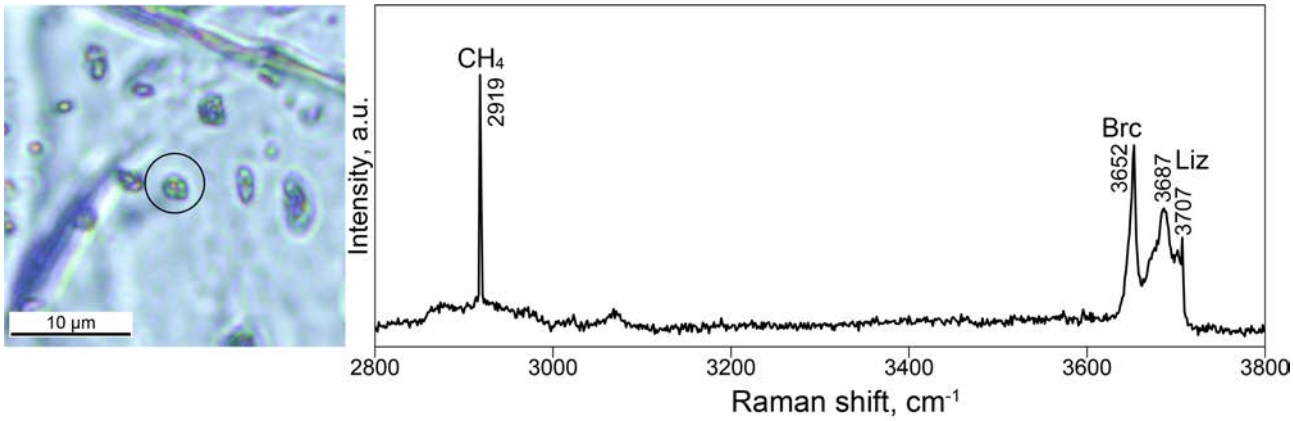
10 μm
CH4
2919
Brc
3652
3687
Liz
3707
Intensity, a.u.
2800
3000
3200
3400
3600
3800
Raman shift, cm-1

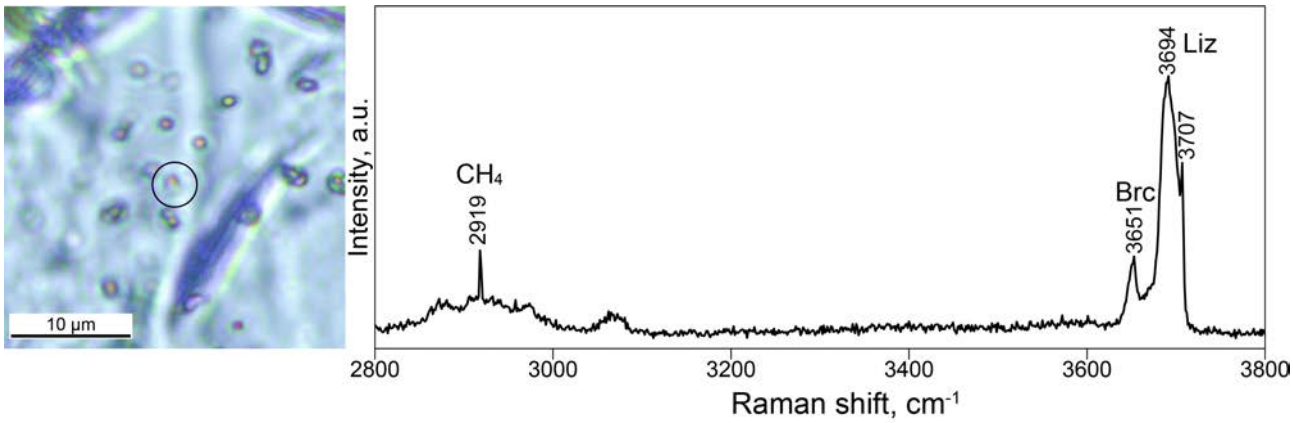
10 μm
CH4
2919
3694
Liz
3707
Brc
3651
Intensity, a.u.
2800
3000
3200
3400
3600
3800
Raman shift, cm-1

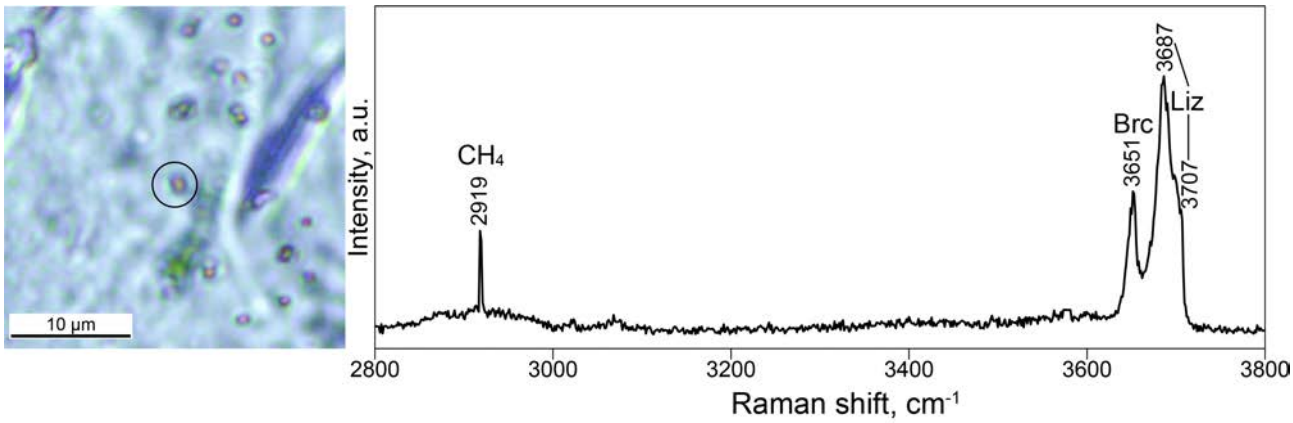
10 μm
CH4
2919
3687
Liz
Brc
3651
3707
Intensity, a.u.
2800
3000
3200
3400
3600
3800
Raman shift, cm-1

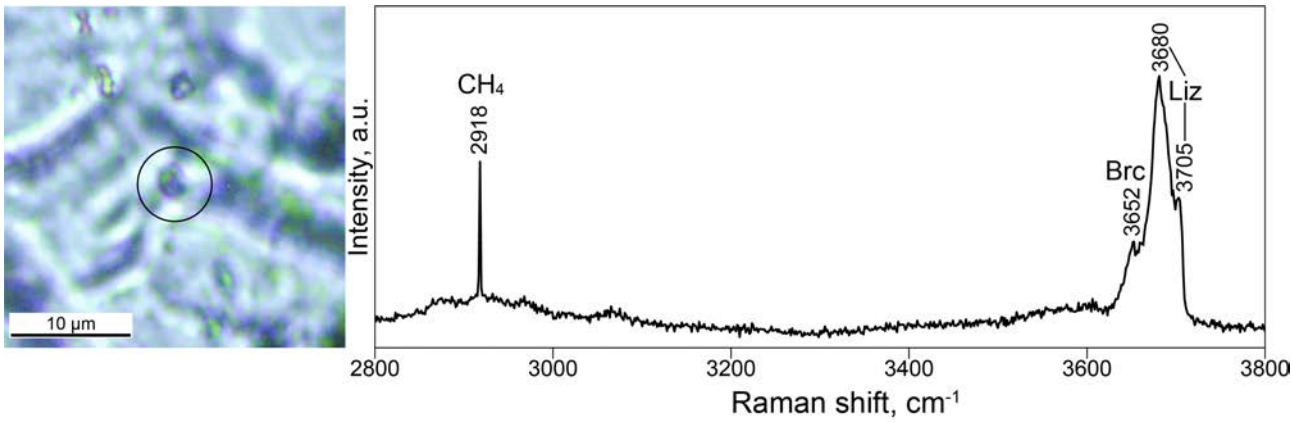
10 μm
CH4
2918
3680
Liz
Brc
3652
3705
Intensity, a.u.
2800
3000
3200
3400
3600
3800
Raman shift, cm-1

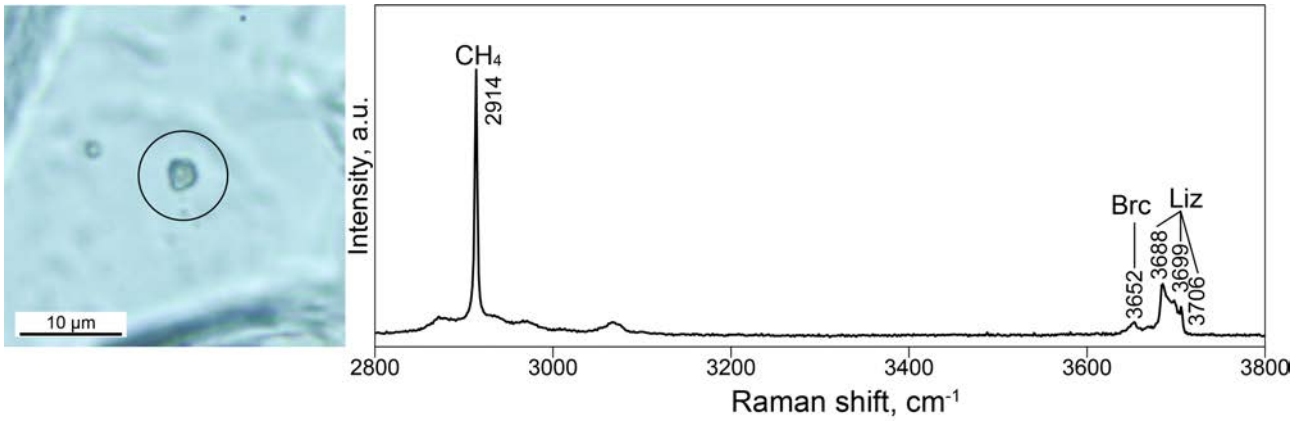
10 μm
CH4
2914
Brc
Liz
3652
3688
3699
3706
Intensity, a.u.
2800
3000
3200
3400
3600
3800
Raman shift, cm-1

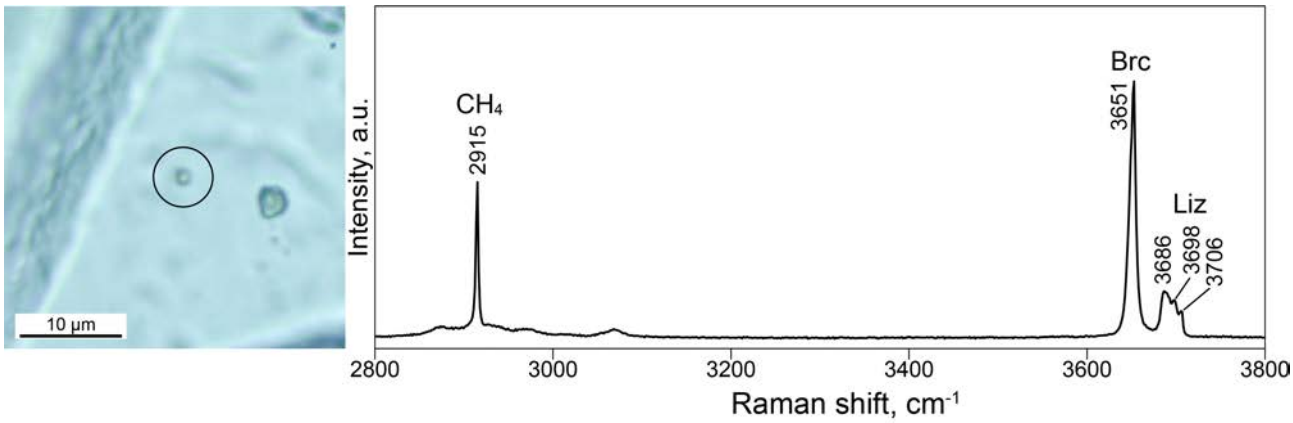
10 μm
CH4
2915
Brc
3651
Liz
3686
3698
3706
Intensity, a.u.
2800
3000
3200
3400
3600
3800
Raman shift, cm-1

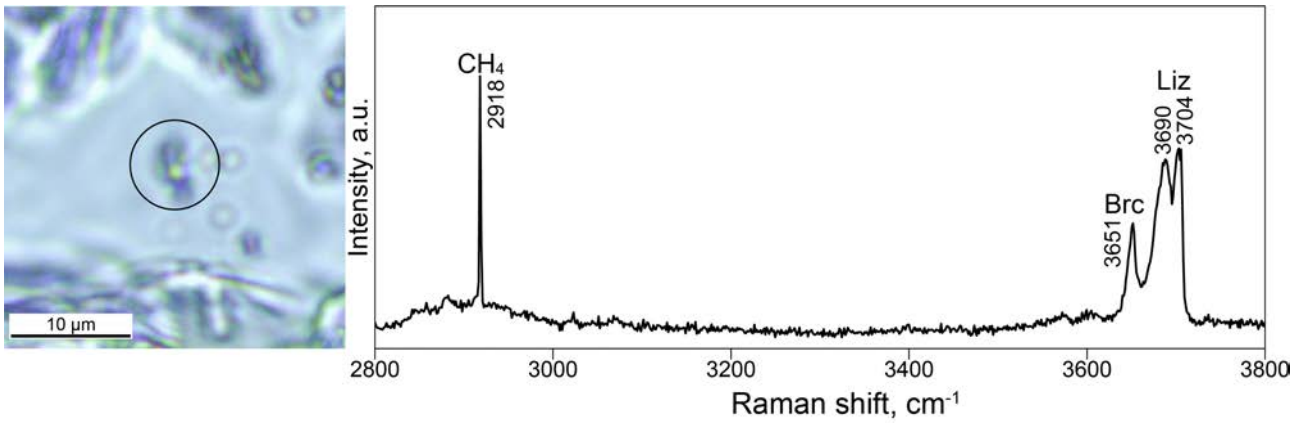
10 μm
CH4
2918
Liz
3690
3704
Brc
3651
Intensity, a.u.
2800
3000
3200
3400
3600
3800
Raman shift, cm-1

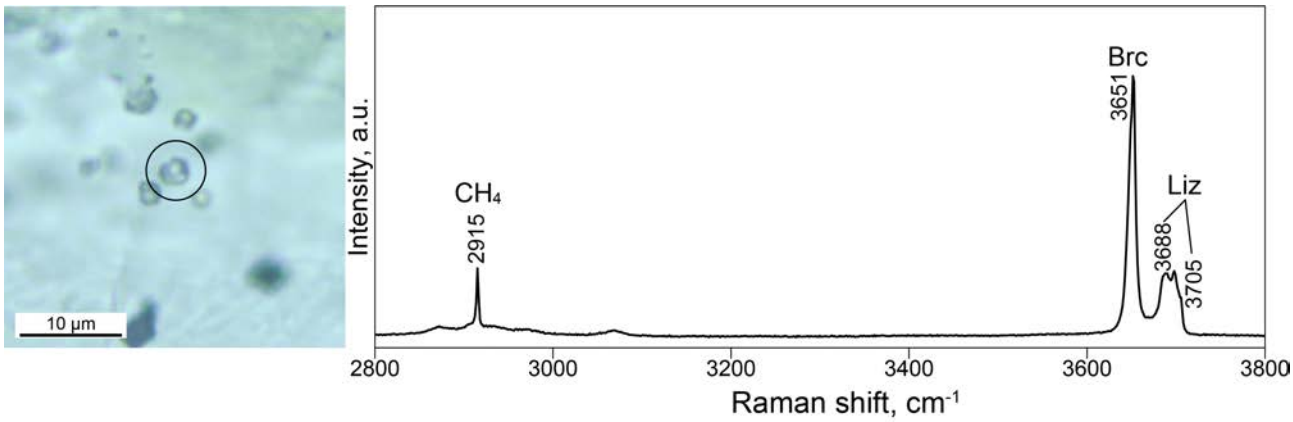
10 μm
CH4
2915
Brc
3651
Liz
3688
3705
Intensity, a.u.
2800
3000
3200
3400
3600
3800
Raman shift, cm-1

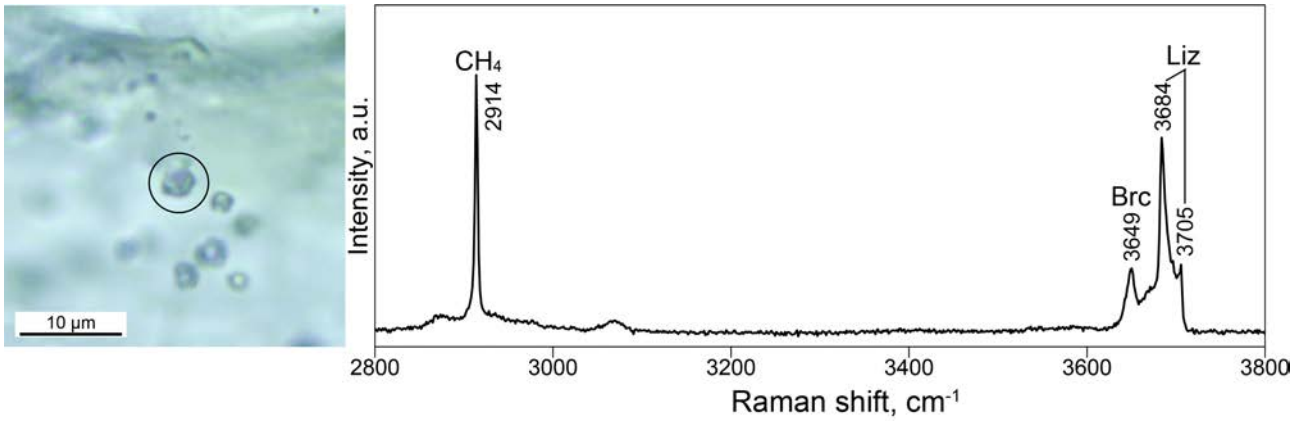
10 μm
CH4
2914
Liz
3684
Brc
3649
3705
Intensity, a.u.
2800
3000
3200
3400
3600
3800
Raman shift, cm-1

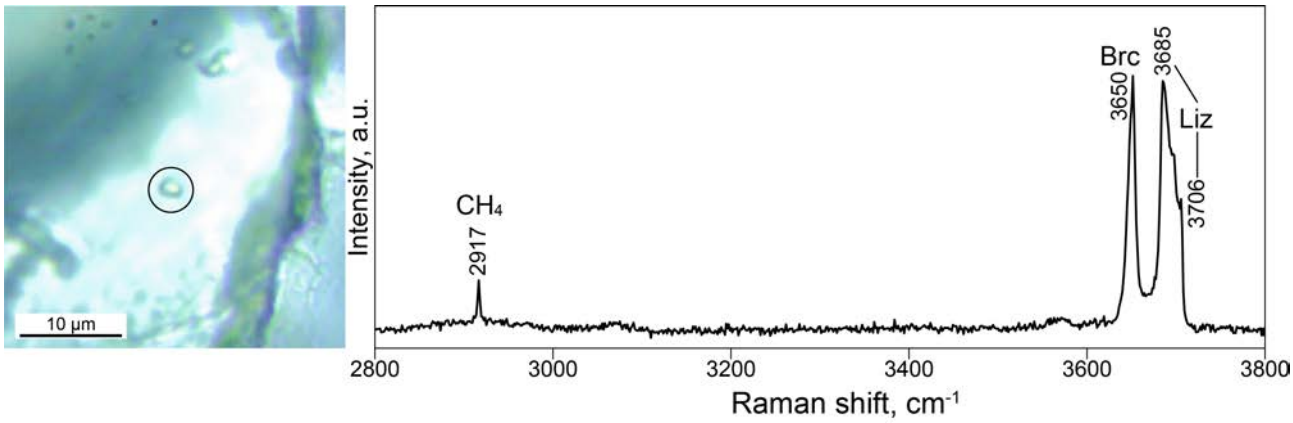
10 μm
Brc
3650
3685
Liz
3706
CH4
2917
Intensity, a.u.
2800
3000
3200
3400
3600
3800
Raman shift, cm-1

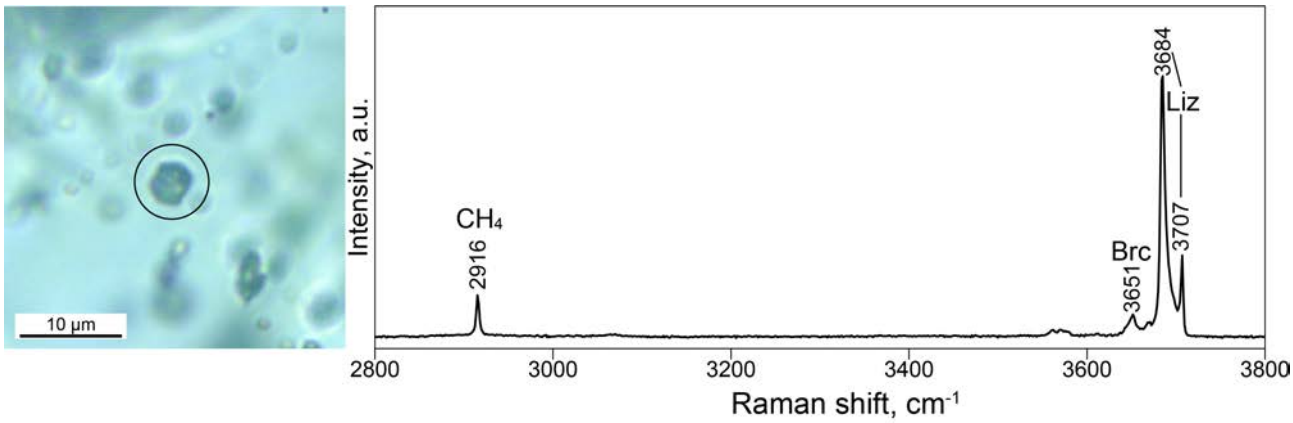
10 μm
3684
Liz
3707
CH4
2916
Brc
3651
Intensity, a.u.
2800
3000
3200
3400
3600
3800
Raman shift, cm-1

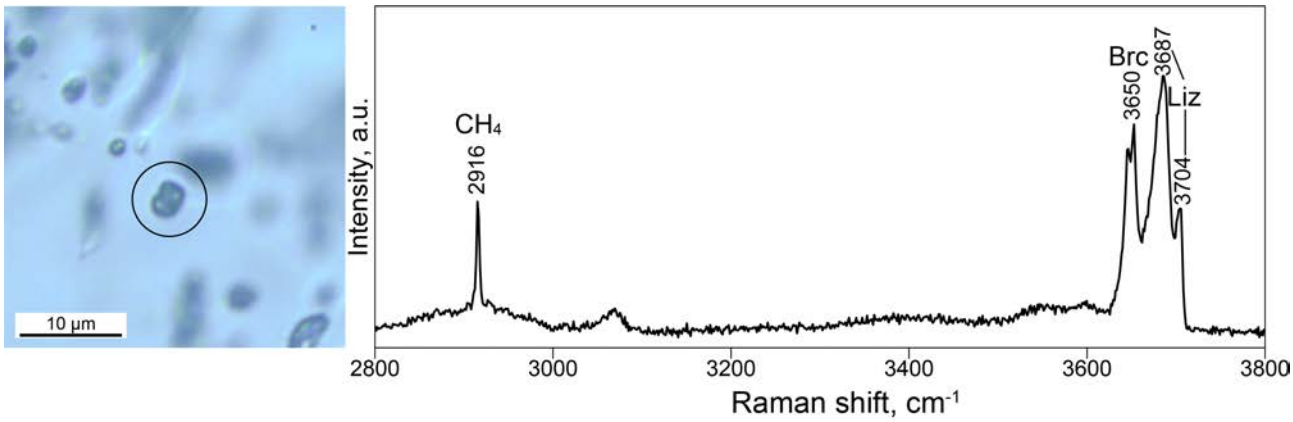
10 μm
Brc
3650
3687
Liz
3704
CH4
2916
Intensity, a.u.
2800
3000
3200
3400
3600
3800
Raman shift, cm-1

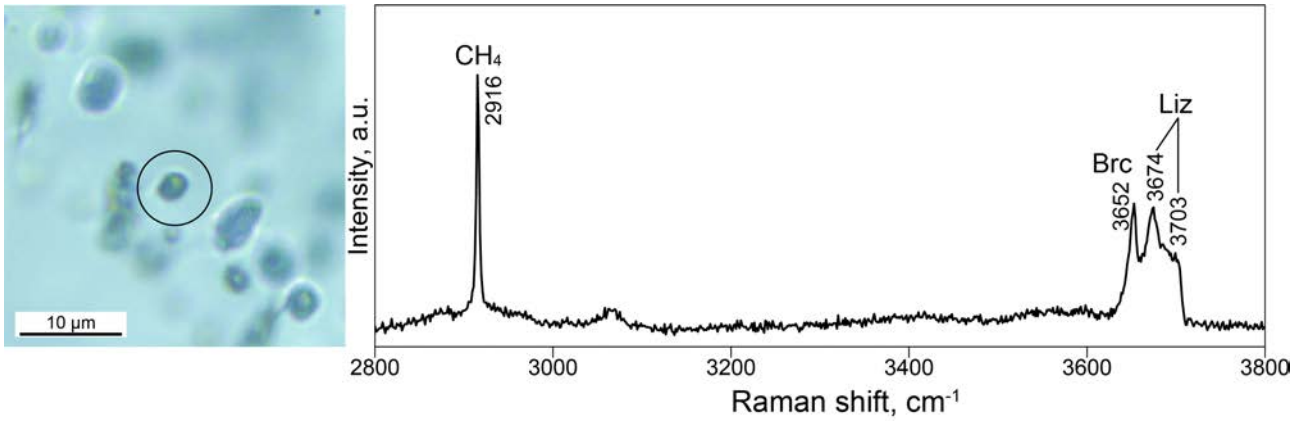
10 μm
CH4
2916
Liz
Brc
3652
3674
3703
Intensity, a.u.
2800
3000
3200
3400
3600
3800
Raman shift, cm-1

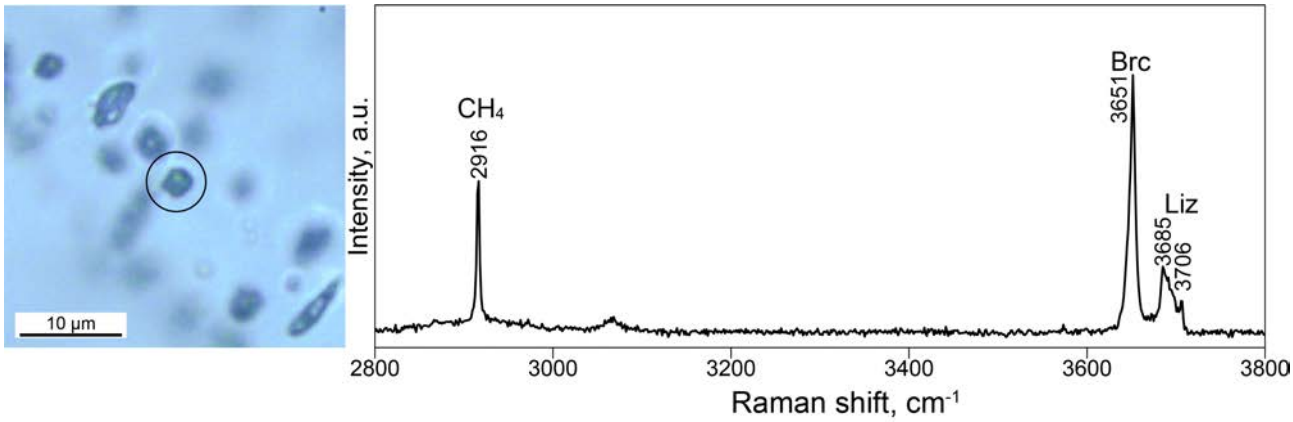
10 μm
CH4
2916
Brc
3651
Liz
3685
3706
Intensity, a.u.
2800
3000
3200
3400
3600
3800
Raman shift, cm-1

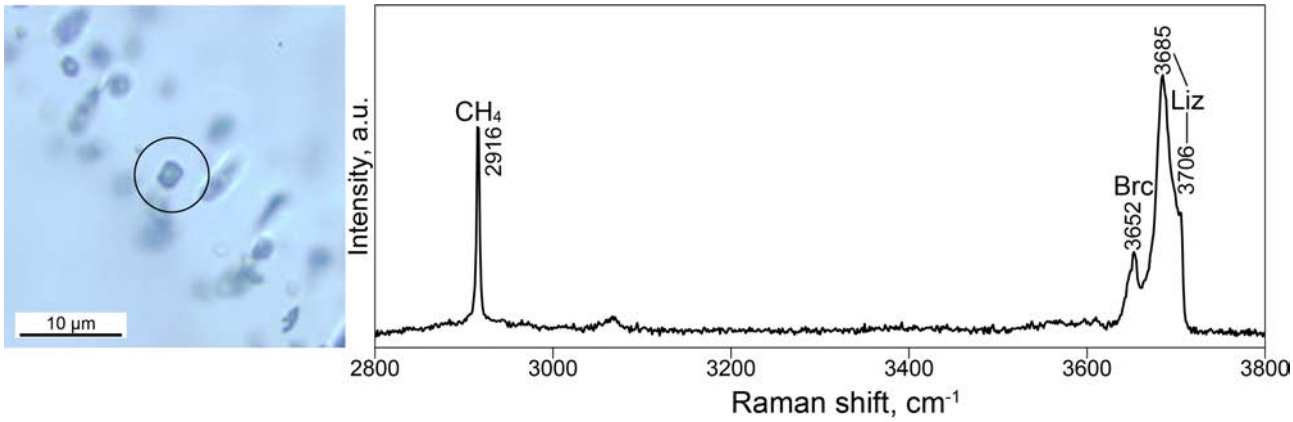
10 μm
CH4
2916
3685
Liz
3706
Brc
3652
Intensity, a.u.
2800
3000
3200
3400
3600
3800
Raman shift, cm-1

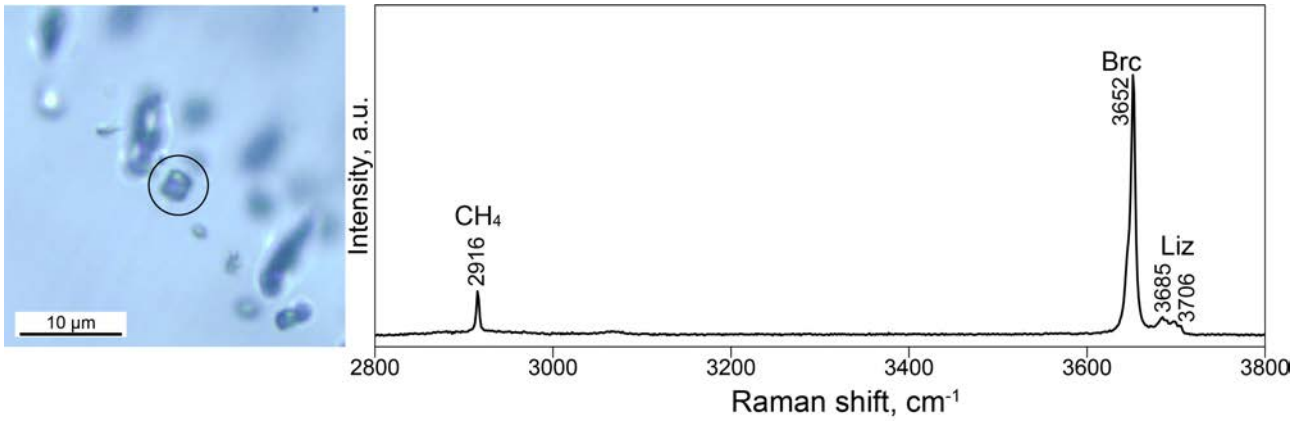
10 μm
CH4
2916
Brc
3652
Liz
3685
3706
Intensity, a.u.
2800
3000
3200
3400
3600
3800
Raman shift, cm-1

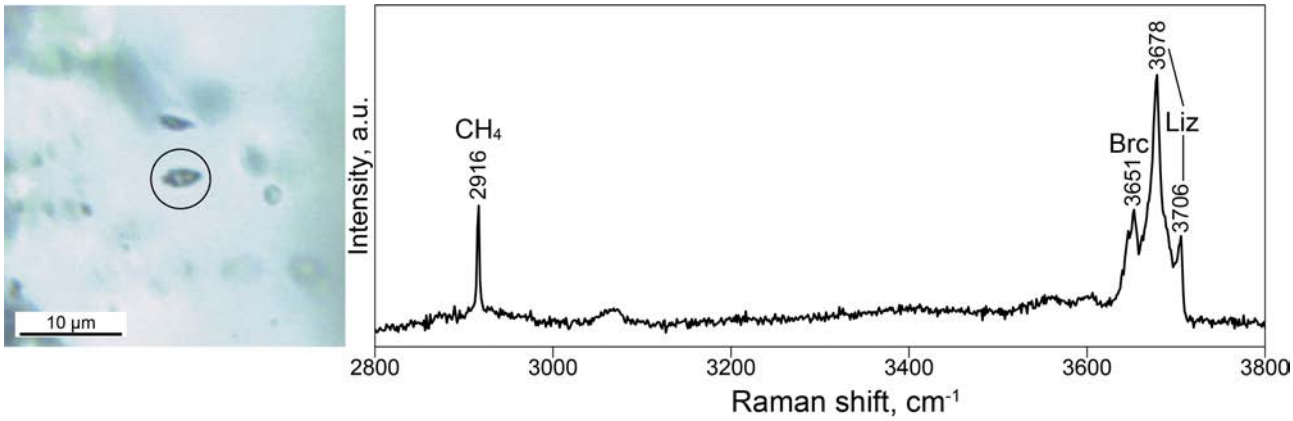
10 μm
CH4
2916
Brc
3651
3678
Liz
3706
Intensity, a.u.
2800
3000
3200
3400
3600
3800
Raman shift, cm-1

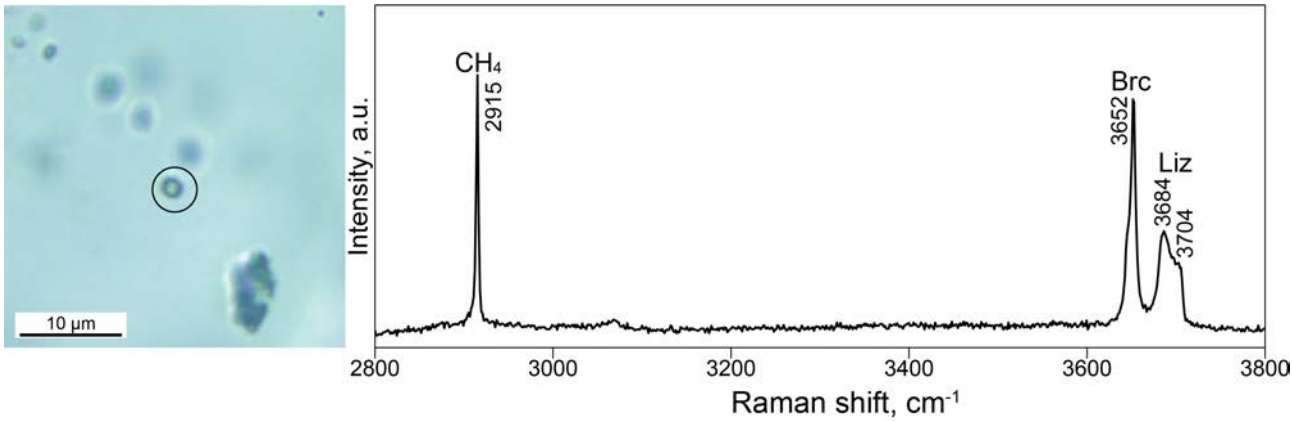
10 μm
CH4
2915
Brc
3652
Liz
3684
3704
Intensity, a.u.
2800
3000
3200
3400
3600
3800
Raman shift, cm-1

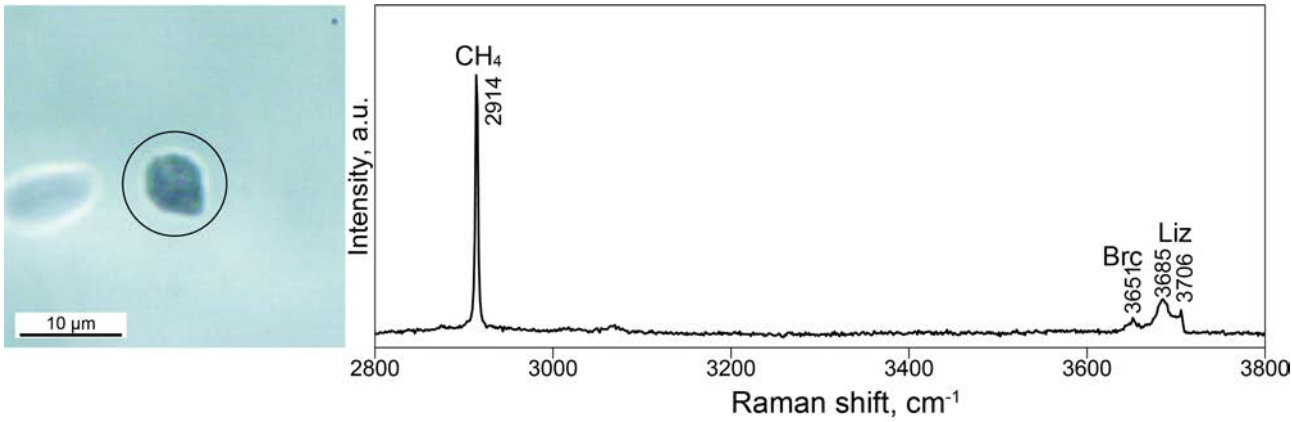
10 μm
CH4
2914
Brc
3651
Liz
3685
3706
Intensity, a.u.
2800
3000
3200
3400
3600
3800
Raman shift, cm-1

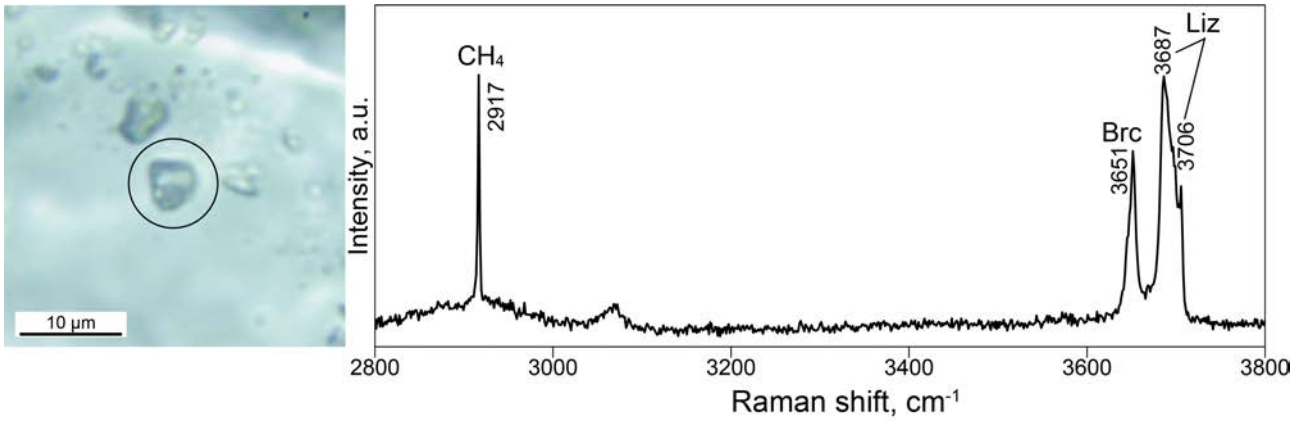
10 μm
CH4
2917
Brc
3651
3687
Liz
3706
Intensity, a.u.
2800
3000
3200
3400
3600
3800
Raman shift, cm-1

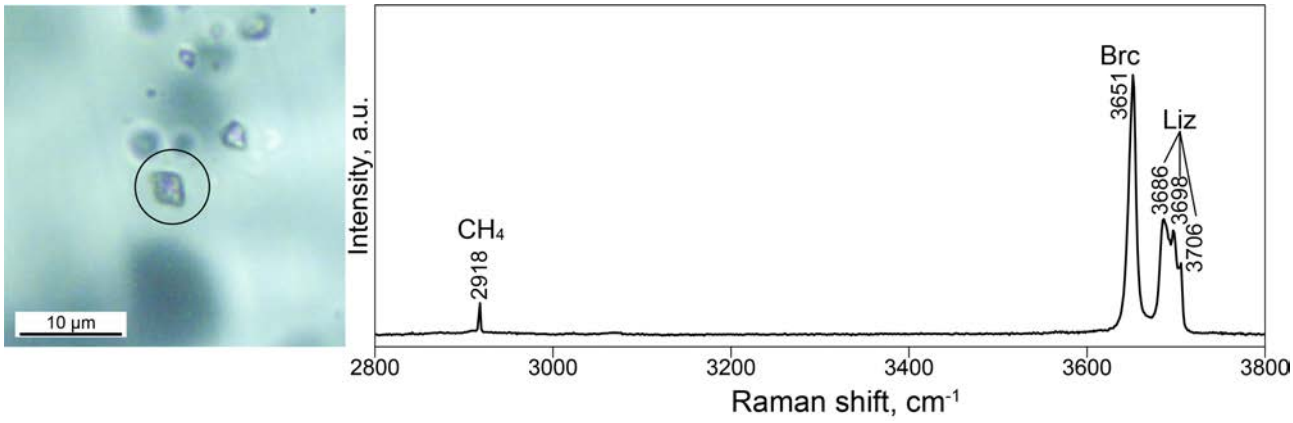
10 μm
Intensity, a.u.
CH4
2918
Brc
3651
Liz
3686
3698
3706
2800
3000
3200
3400
3600
3800
Raman shift, cm-1

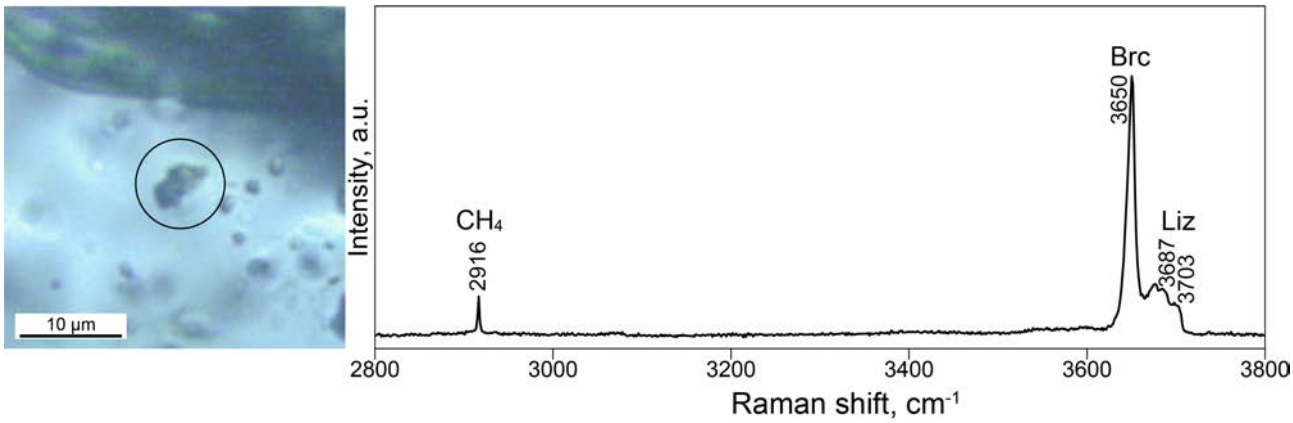
10 μm
Intensity, a.u.
CH4
2916
Brc
3650
Liz
3687
3703
2800
3000
3200
3400
3600
3800
Raman shift, cm-1